Bridging Behavior of Palm Fiber in Fiber-Reinforced Cementitious Composite

SELAMAWIT FTHANEGEST ABRHA

(Master's Program in Engineering Mechanics and Energy)

Advised by Toshiyuki Kanakubo

Submitted to the Graduate School
of Science and Technology
Degree Programs in Systems and
Information Engineering
in Partial Fulfillment of the Requirements
for the Degree of Master of Engineering
at the
University of Tsukuba

March 2024

Abstract

Fiber-reinforced cementitious composites (FRCCs) are a type of material that combines the benefits of cement-based composites with the addition of fibers to enhance its mechanical properties. Incorporating natural fiber in FRCC represents a sustainable and promising avenue for enhancing cement-based materials' mechanical and environmental performance. The use of natural fiber in FRCC is not without a challenge, so a widespread application of natural fiber in the construction industry needs an understanding of the synergies between fibers and cementitious matrices. This research aims to develop a reliable and effective bridging law for assessing the tensile performance of FRCC incorporating palm fiber by using a single fiber pullout test.

The palm fiber was prepared by cutting a palm rope with a shredder. The density of the fiber was measured by Archimedes' principle which states that the volume of liquid displaced is equal to the volume of an object completely immersed in liquid. The average density is $0.723 g/cm^3$. A scanning electron microscope (SEM) was used to observe the surface configuration and measure the diameter of the fiber where the average diameter is $171 \mu m$.

A total of 57 specimens were subjected to single fiber pullout tests. The embedded length (2, 4, and 6mm) and fiber inclination angle (0, 15, 30, 45, and 60°) were the main parameters. The relationship between the first peak load and the maximum pullout load with embedded length and orientation angle was examined based on the experimental results. Snubbing effects were considered for the first peak load and maximum pullout load. The pullout behavior was modeled using the trilinear model. A bridging model for palm fiber was constructed using the bridging law calculation derived from the single-fiber pullout model.

A tensile stress–crack width relationship model for palm-FRCC was created using the bridging law calculation based on the trilinear model. Section analysis is conducted to assess the adaptability of the modeled bridging law calculations. The analysis result of the bending moment–curvature relationship shows good agreement with the experimental results obtained from the 4-point bending test of palm-FRCC.

Contents

List of Figures

List of Tables

Chapter 1 Introduction

1.1 Fiber-Reinforced Cementitious Composite (FRCC)

Concrete's tensile strength is considerably smaller than its compressive strength and exhibits a highly brittle nature. In reinforced concrete (RC) structures, it is commonly conceptualized that concrete bears compressive forces while reinforcing bars bear tensile forces. Brittle failure in RC members is often attributed to the tensile failure of concrete. Research on fiber-reinforced cementitious composite (FRCC) has been conducted extensively over the years to enhance the tensile ductility of concrete.

FRCCs are a type of material that combines the benefits of cement-based composites with the addition of fibers to enhance their mechanical properties. These composites exhibit improved ductility during bending, tension, and compression failures. Incorporating fibers into the cementitious matrix helps to enhance the tensile strength and ductility of the material, which are typically lacking in conventional concrete materials [1].

Over the past few decades, researchers have introduced and studied various types of FRCCs, including engineered cementitious composites, strain-hardening cement composites, and ductile fiber-reinforced cementitious composites. These composites have shown strain hardening and/or deflection hardening with multiple cracking behaviors, making them suitable for structural applications that require improved durability and resistance to cracking [2].

Fiber reinforcement in cementitious composites has been a widely used and effective method to enhance the toughness and durability of cement-based products. The performance of FRCCs depends on several factors, such as the properties of the fiber material, fiber geometry, fiber volume fraction, matrix properties, and interface properties.

1.2 Natural Fiber in Fiber-Reinforced Cementitious Composite

Unprocessed or treated natural fibers have found applications in reinforcing cement-based products globally. These fibers, derived from various parts of plants, such as jute, ramie, flax, kenaf, and hemp from stems, and sisal, banana, and pineapple from leaves, as well as cotton and kapok from seeds, have been utilized in diverse applications. Natural fibers are composites with a cellular structure including different proportions of cellulose, hemicellulose, and lignin which constitute different layers [3].

Natural fibers, sourced from renewable materials like plants (e.g., jute, sisal, hemp) or animals (e.g., wool), offer inherent advantages as reinforcements in cementitious composites. Biodegradability is a notable feature, aligning with the global shift towards environmentally friendly construction practices. Additionally, the use of natural fibers contributes to reduced energy consumption and carbon emissions compared to the production of artificial fibers traditionally employed in cementitious composites.

Natural fibers integrated into FRCCs present a significant stride towards sustainable and environmentally conscious construction materials. Traditional cementitious composites often grapple with brittleness and a lack of ductility, issues that the incorporation of natural fibers aims to mitigate.

The integration of natural fibers in FRCC provides a potential solution to the challenges associated with conventional reinforcement materials. Current research underscores the promising outcomes in terms of increased flexural strength, fracture toughness, and ductility. The improved bending and tensile strength, coupled with greater resistance to cracking, contribute to enhanced overall strength and toughness [4].

Natural fibers exhibit low density and high specific strength, rendering them suitable candidates for lightweight construction materials. The reduced density contributes to an overall decrease in the composite's weight, facilitating easier handling, transportation, and installation. This characteristic proves advantageous in weight-sensitive applications, such as infrastructure construction and the retrofitting of existing structures.

One distinctive aspect of natural fibers is their lower cost compared to conventional artificial fibers, making them a more economically appealing option for non-bearing building materials [5]. This economic advantage further positions natural fiber-reinforced cementitious composites as a practical and cost-effective choice in construction applications.

The use of natural fibers in FRCCs is not without challenges. Issues such as fiber-matrix compatibility, fiber dispersion, and long-term durability must be carefully addressed to ensure optimal performance.

1.3 Pullout Behavior of Single Fiber

1.3.1 Bridging law

FRCCs have emerged as advanced materials with enhanced mechanical properties, durability, and ductility compared to traditional cement-based materials. The incorporation of various fibers, such as polymeric, metallic, or glass fibers, has significantly contributed to the improvement of tensile performance in FRCC. One critical aspect of understanding and optimizing the tensile behavior of FRCC is the application of bridging law principles.

The bridging law concept plays a pivotal role in explaining the tensile behavior of FRCC. Bridging refers to the ability of fibers to span across cracks and distribute loads, thereby impeding crack propagation and enhancing the material's post-cracking performance [6]. In FRCC, the bridging law is a theoretical framework that describes the relationship between crack opening displacement and the applied load.

The bridging law calculates the bridging stress by summing up the behaviors of individual fibers pulled out experimentally and bridging them across multiple fibers on the crack surface [7]. By utilizing the bridging rule, it is possible to evaluate the tensile properties of FRCC based on material constituents such as fiber-matrix adhesion characteristics and fiber fracture strength. Figure 1.1 shows the performance evaluation of structural FRCC members using bridging law and the material design that spans from the micro to macro level.

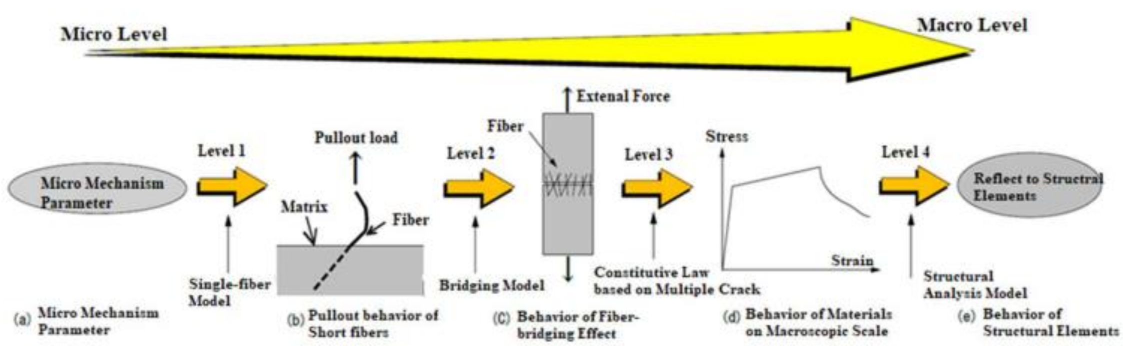

Figure 1.1 Flow of material design [8]

Tensile performance is affected by many factors such as fiber type and content, fiber orientation and distribution, matrix property, and crack width. Different fibers exhibit distinct mechanical properties and bonding characteristics with the matrix. The type and content of fibers significantly influence the bridging mechanism and, consequently, the tensile performance of FRCC.

Since the pullout behavior of single fibers is fundamental in the bridging rule, a more precise evaluation is demanded. Furthermore, as the pullout behavior varies significantly depending on the type of fibers and matrix, it is necessary to construct specific bridging rules for the targeted FRCC.

1.3.2 Pullout behavior

In FRCC, fibers are oriented in various directions and when cracks occur, fibers with angles bridge the cracks. The angle of the fibers in this case is referred to as the orientation angle. The pullout behavior of single fibers is influenced by the adhesion characteristics between the fiber and matrix, based on which the impact of the fiber orientation angle is considered.

Typically, when fibers have an orientation angle, the pullout force increases due to reactive forces from the matrix at the embedding point of the fiber as shown in Figure 1.2. This increase in pullout force when fibers have such an inclination angle is known as the snubbing effect, and it is believed to increase with a larger orientation angle [9]. The snubbing effect is expressed as a snubbing coefficient using Equation (1.1) as an indicator of the degree of increase in the maximum load.

$$P = P_0 \cdot e^{f\theta} \tag{1.1}$$

Where,

P = pullout load

P_0 = pullout load when the orientation angle is 0°

θ = fiber orientation angle.

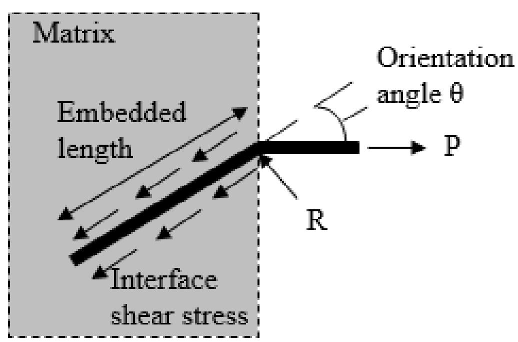

Figure 1.2 Pullout resistance mechanism of single fiber

Furthermore, previous studies have confirmed a phenomenon known as fiber strength reduction due to the roughening of the fiber surface [10]. This phenomenon is called the fiber strength reduction effect and is expressed by Equation (1.2) using the fiber strength reduction coefficient f'.

$$\sigma_{fu} = \sigma^{n}{}_{fu} \cdot e^{-f'\theta} \tag{1.2}$$

Where,

σ_{fu} = apparent fiber strength

$\sigma^{n}{}_{fu}$ = apparent fiber strength when the orientation angle is 0°

f' = fiber strength reduction coefficient.

θ = fiber orientation angle.

The snubbing coefficient f and the fiber strength reduction coefficient f' are determined from the results of single fiber pullout experiments. As shown in Figure 1.2, the pullout force increases due to the snubbing effect as the orientation angle increases, and the fiber ruptures when the orientation angle further increases.

1.4 Research Objective

FRCCs have gained significant attention in recent years due to their enhanced mechanical properties and durability. One type of natural fiber that has shown promise in reinforcing cementitious materials is palm fiber. Extracted from various species of palm trees, this renewable and biodegradable material has unique characteristics that make it an attractive choice for improving the performance of cement-based composites [11].

Palm fibers are characterized by their high aspect ratio, low density, and biodegradability. These fibers possess excellent tensile strength and modulus, contributing to their ability to effectively reinforce cementitious matrices [12]. The mechanical properties of palm fibers make them suitable for enhancing the ductility and toughness of cement-based materials, which are crucial factors in preventing brittle failure.

Moreover, palm fibers exhibit good compatibility with the alkaline environment of cement, mitigating concerns related to chemical degradation over time. Their hydrophilic nature allows for effective bonding with the cementitious matrix, promoting load transfer between the fibers and the surrounding material [13].

The use of palm fiber in FRCCs represents a sustainable and promising avenue for enhancing the mechanical and environmental performance of cement-based materials [14]. Despite the promising attributes of palm fiber, challenges such as fiber dispersion and variability in mechanical properties along with improved understanding of the synergies between palm fibers and cementitious matrices need to be addressed for widespread adoption.

According to this situation, the primary research objective is to advance the use of palm fiber in FRCC by conducting a comprehensive investigation into the tensile performance of FRCC incorporating palm fiber. This entails a deeper understanding of how well the material can withstand stretching forces.

The method for assessing tensile performance is through the application of a bridging law. This law is fundamentally rooted in the performance of the fibers acting as bridges across cracks within the matrix. It essentially quantifies the tensile force that a fiber can withstand while bridging a crack, considering the width of the crack as a crucial parameter.

To achieve this objective, the research focuses on constructing and refining the bridging law, aiming to establish a clear relationship between the tensile force exerted by the palm fibers and the width of the cracks they bridge. This involves a detailed analysis of the bridging performance of the fibers in the FRCC.

The foundational aspect of the bridging law is dependent on the behavior of fibers as they pull out from the matrix. Therefore, a critical component of the research involves conducting single-fiber pullout tests to observe and understand the pullout behavior. By systematically investigating how single fibers interact with and are pulled out from the matrix, the research aims to provide valuable insights into constructing an effective and reliable bridging law for assessing the tensile performance of FRCC with palm fiber.

Chapter 2 Fiber Characterization

2.1 Fiber Type

The fiber type used in this research is palm fiber. Palm fiber is a natural, renewable, and biodegradable material derived from the leaves or husks of palm trees, particularly from oil palm and coconut trees. The incorporation of palm fiber in fiber-reinforced cementitious composites (FRCC) offers a sustainable alternative to traditional reinforcements, contributing to the development of eco-friendly construction materials. The use of palm fiber in FRCC introduces unique properties and challenges that are worth exploring.

A palm fiber was prepared by cutting a palm rope using a 10mm shredder as shown in Figure 2.1. The properties and characteristics of the fiber are distinguished from scratch and discussed in the next section.

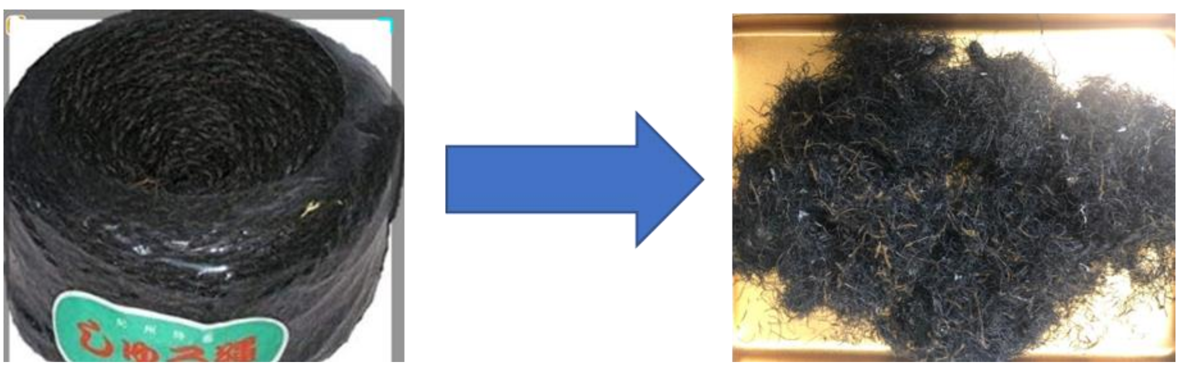

Figure 2.1 Palm fiber

2.2 Density Measurement

Fiber density was calculated using the Archimedes principle. This principle states that the volume of liquid displaced is equal to the volume of an object completely immersed in liquid. The braided palm fibers were sampled before cutting and the dry weight at room temperature was measured. The sample was soaked in water for 22 hours and the wet weight was measured after squeezing. The sample was then immersed in a full glass funnel and the mass of water displaced was measured as the fiber volume. Density calculation methods and results are shown in Figure 2.2 and Table 2.1. The average density is 0.723g/cm³.

Table 2.1 Density of fiber

Sample	Wet weight (g)	Dry weight (g)	Volume (cm^3)	Density (g/cm^3)
1	23.3	14.9	17.9	0.832
2	31.1	16.5	24.9	0.663
3	29.0	16.6	23.9	0.695
4	32.2	16.7	26.7	0.625
5	28.3	17.5	21.9	0.799
Avg.	28.8	16.4	23.1	0.723

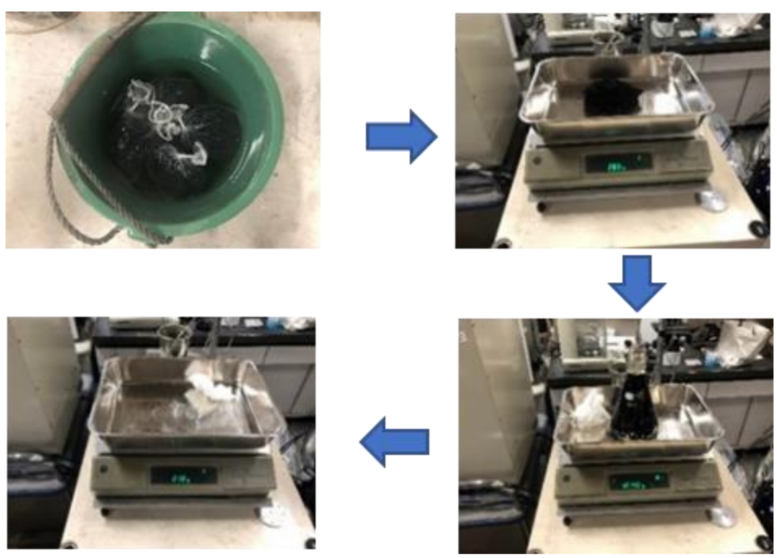

Figure 2.2 Measurement of fiber volume

2.3 Diameter and Morphology using SEM

A scanning electron microscope (SEM) was used to observe the fiber configuration and measure the diameter. All the samples have a cylindrical shape as shown in Figure 2.3a. Figure 2.3b shows the wax and impurities on the surface and Figure 2.3c shows the array of bulges which are silica bodies embedding circular holes. In Figure 2.3d, the silica is removed leaving an empty hole that may facilitate the mechanical interlocking of the fiber and the matrix. Figure 2.4 shows the distribution of fiber diameters, with an average fiber diameter of 171μm.

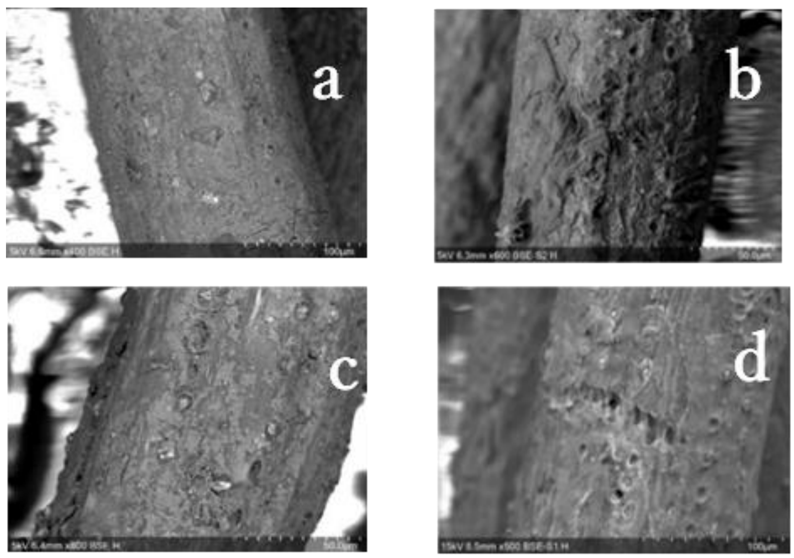

Figure 2.3 Surface observation

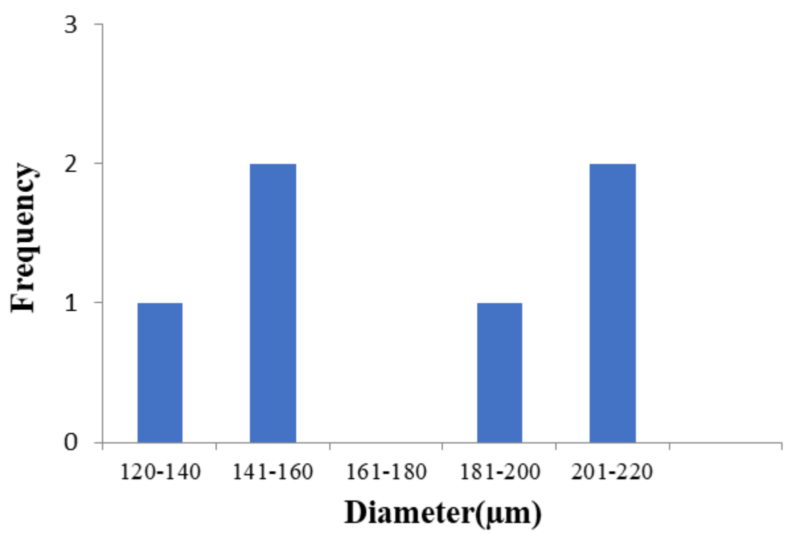

Figure 2.4 Fiber diameter distribution

Chapter 3 Single Fiber Pullout Test

3.1 Experiment Overview

3.1.1 Materials

The palm fiber used in this study is the same as the fiber described in section 2.1. Table 3.1 shows the mixture proportion adopted in this research. To balance the mechanical characteristics of palm fiber with those of matrix, a mixture proportion with compressive strength of 24MPa class was adopted.

Table 3.1 Mixture proportion

W/C	FA/B	Unit weight (kg/m^3)			
		Water	Cement	FA	Sand
0.785	0.5	380	484	484	484

W: Water,

C: Cement (high early-strength Portland cement),

FA: Fly ash (Type II of JIS A 6201),

B: Binder (=C + FA),

S: Sand (size under 0.2 mm).

3.1.2 Specimens

Figure 3.1 shows the mold design and the dimension of the specimen for the pullout test of single palm fiber. The specimen mold consists of three rubber plates sandwiched between two acrylic plates and tightened with bolts. The specimen is formed of a matrix with a single fiber implanted in the center. The dimension of the specimens in the plane section is 30×30mm as shown in Figure 3.1. The embedded length (2, 4, and 6mm) and fiber inclination angle (0, 15, 30, 45, and 60°) are the main parameters for this research. The embedded length of the fiber, which is proportional to the thickness of the specimen, is adjusted by changing the thickness of the rubber plate at the center. Table 3.2 shows the list of parameters and the number of specimens adopted in this research.

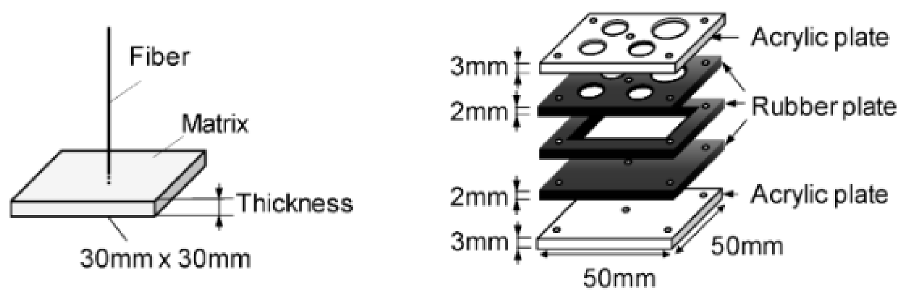

Figure 3.1 Specimen for pullout test

Table 3.2 List of specimens

Specimen name	Embedded length (mm)	Inclination angle (°)	No. of specimen
P-2mm-0	2	0	5
P-2mm-15		15	5
P-2mm-30		30	5
P-2mm-45		45	5
P-2mm-60		60	5
P-4mm-0	4	0	5
P-4mm-15		15	5
P-4mm-30		30	5
P-4mm-45		45	5
P-4mm-60		60	5
P-6mm-0	6	0	5
P-6mm-15		15	5
P-6mm-30		30	5
P-6mm-45		45	5
P-6mm-60		60	5

3.1.3 Loading and measurement

A single fiber pullout test was conducted using an electronic system universal testing machine (LSC-02/30-2, Tokyo Testing Machine Co., Ltd., Tokyo Japan) with a capacity of 200N. As shown in Figure 3.2 the specimen was attached to a steel plate prepared for each inclination angle by bolting the steel plate bonded to the specimen, and the single fiber was directly clamped by the gripping jig. The fiber length out of the matrix was set to 50mm. The pullout load and head displacement were recorded.

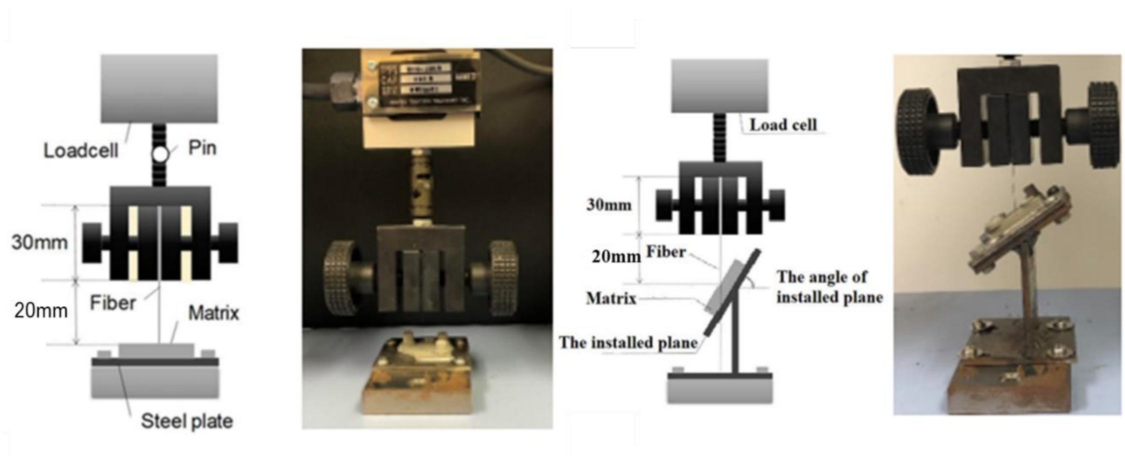

(a) (b)

Figure 3.2 Pullout test setup

(a)Specimen at 0 inclination angle, (b)Specimen with inclination angle

3.2 Experimental Result

3.2.1 Uniaxial tension test for single palm fiber

Preliminary to the single fiber pullout test, a uniaxial tension test was conducted on a single palm fiber to derive an expression for predicting the elongation of the fiber outside the matrix. This test involved a single fiber pullout analysis in which the slip was determined by subtracting the elongation of the fiber outside the matrix from the head displacement. Thirty sample fibers were subjected to testing.

The fiber was directly clamped by the chunking jig at both ends and the fiber length was 100mm, which is twice the length outside the matrix section in the single fiber pullout test. A monotonic tensile loading was applied using an electronic system universal testing machine as shown in Figure 3.3.

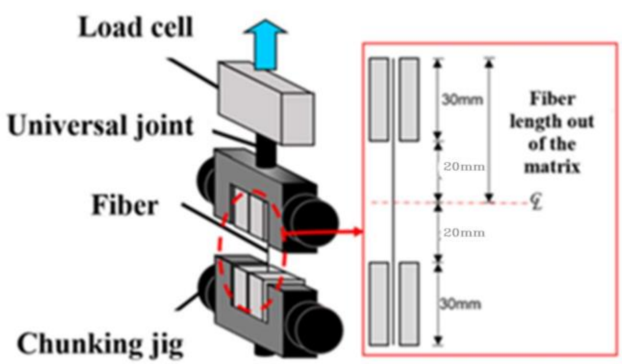

Figure 3.3 Uniaxial tension test setup for single fiber

Figure 3.4 shows the results of the uniaxial tension test and the approximate equation of the tensile load-head displacement relationship for each test result. The approximate equation of the tensile load-head displacement relationship up to the maximum load for each test result was obtained by the least-squares method. In the figure, the solid line represents the test results, while the dashed lines depict the approximations for each specimen. It is assumed that the variability in the test results occurred due to the difference in fiber diameter, the chemical composition of the fiber, and the section of extraction of the fiber. Some show an increase and decrease in the tensile load, this is assumed to be due to the decomposition of the cellulose microstructure of the palm fiber.

The red curve in Figure 3.5 is computed by averaging the coefficients from these approximations as given in Equation (3.1). Given that the fiber under investigation is a natural cellulose material with varying diameters, it is evident from the Figure that the averaged curve lacks inclusivity for all tested sample fibers. Therefore, an alternative approach is adopted wherein, instead of an averaged curve, the elongation at P=0.5N is determined for each fiber based on the uniaxial tension test results. The equation with the closest correspondence to the displacement at P=0.5N in the pullout test is selected as the method for calculating fiber elongation outside the embedded region in the pullout test.

Half of the value computed from the equations estimates the elongation of the fiber outside the embedment region in the pullout test. This value is then subtracted from the measured head displacement to correct for relative displacement, as outlined in Equation (3.2).

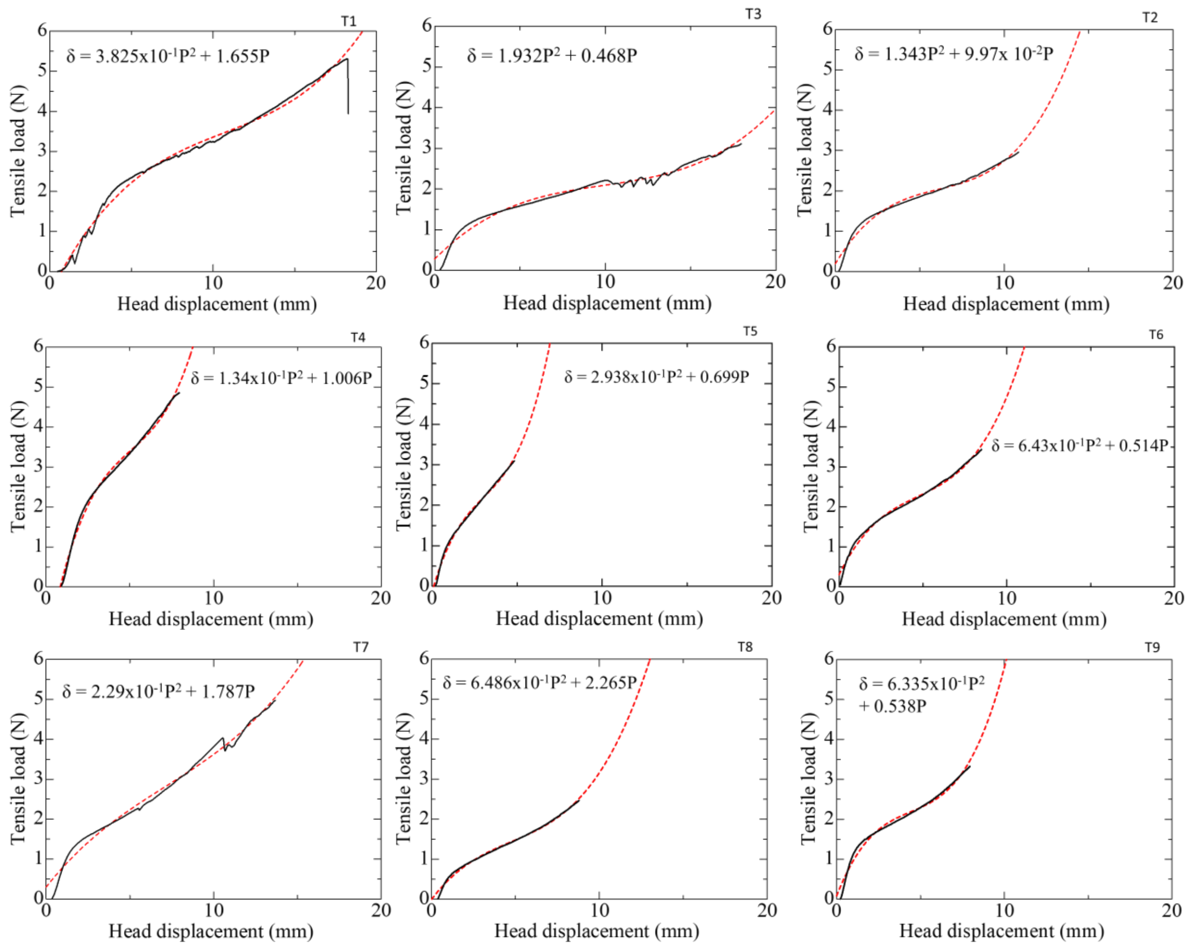

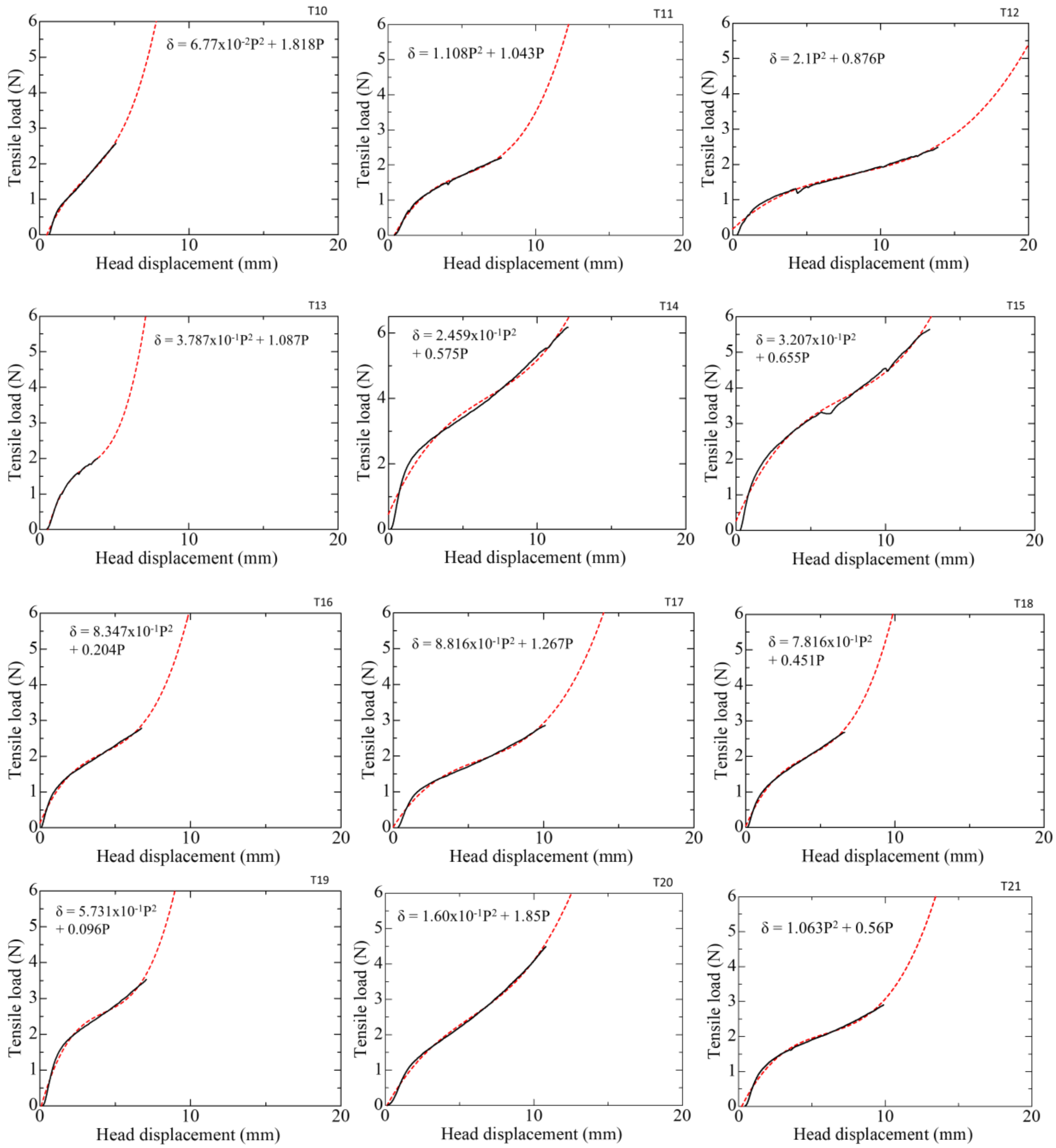
T10
δ = 6.77x10⁻²P² + 1.818P
T11
δ = 1.108P² + 1.043P
T12
δ = 2.1P² + 0.876P
T13
δ = 3.787x10⁻¹P² + 1.087P
T14
δ = 2.459x10⁻¹P² + 0.575P
T15
δ = 3.207x10⁻¹P² + 0.655P
T16
δ = 8.347x10⁻¹P² + 0.204P
T17
δ = 8.816x10⁻¹P² + 1.267P
T18
δ = 7.816x10⁻¹P² + 0.451P
T19
δ = 5.731x10⁻¹P² + 0.096P
T20
δ = 1.60x10⁻¹P² + 1.85P
T21
δ = 1.063P² + 0.56P
Tensile load (N)
Head displacement (mm)

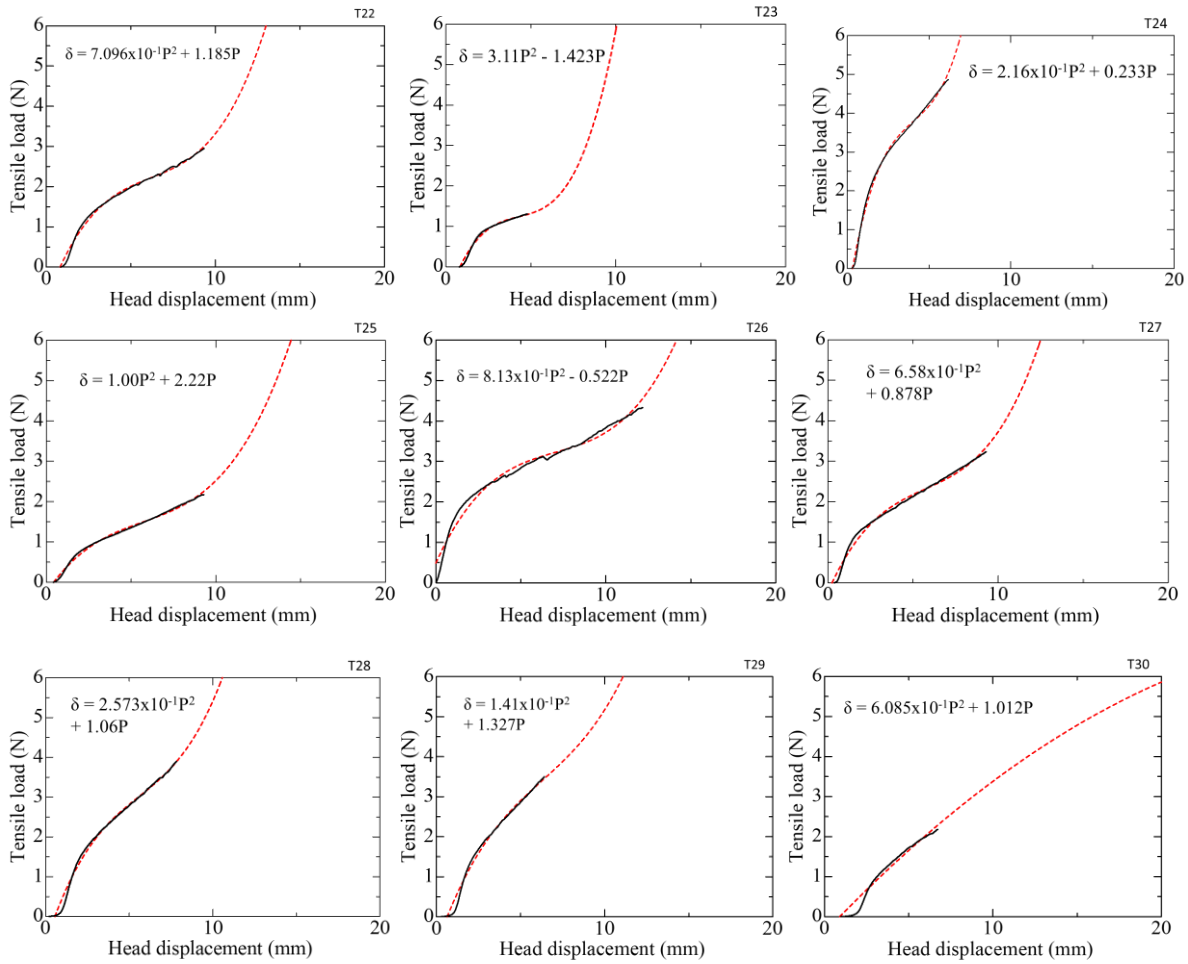

Figure 3.4 Uniaxial tension test result

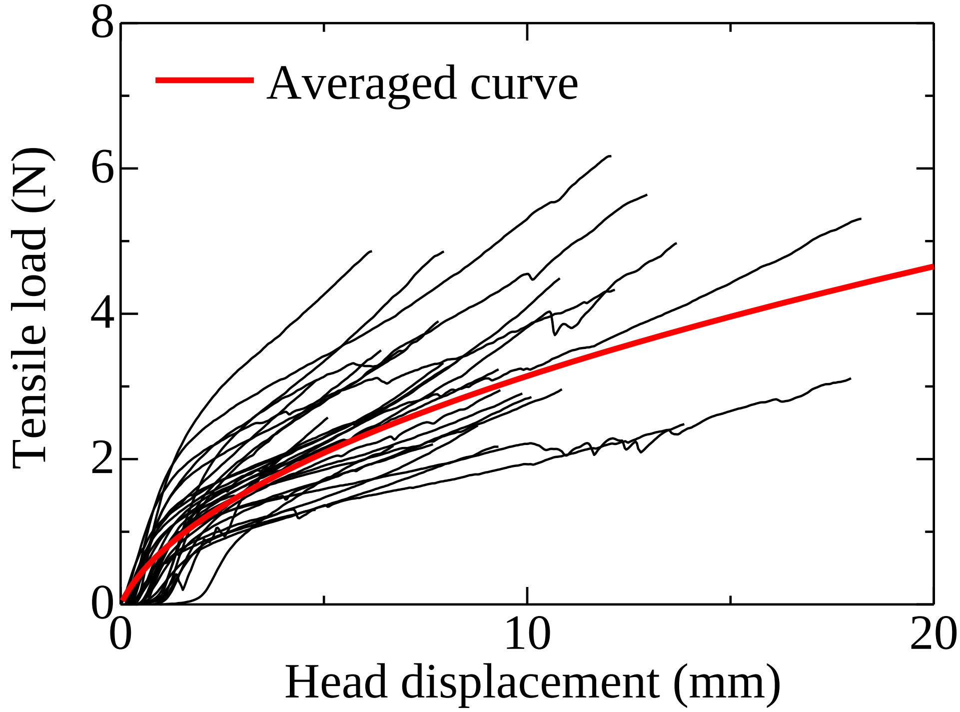

Figure 3.5 Tensile load - head displacement

$$\delta = 7.42 \times 10^{-1} P^2 + 8.49 \times 10^{-1} P \tag{3.1}$$

$$s = x - \delta/2 \tag{3.2}$$

Were,

P: pullout load (N)
s: slip (mm)
x: recorded head displacement (mm)

3.2.2 Single fiber pullout test

The head displacement obtained from the pullout test includes the elongation of fibers outside the embedded region in the matrix. To correct for the relative displacement between the matrix and fibers, the corrected displacement obtained from the uniaxial tension test is used to adjust the slip, as per Equations (3.2). The corrected pullout load (P) - slip (s) relationship obtained from the pullout test is shown in Figures 3.6 to 3.8. After completing the loading of each specimen, the thickness of the embedded length near the fiber pore was measured using calipers (indicated in Tables 3.3 to 3.5). A clear fiber rupture or matrix damage was not observed in the single fiber pullout test. A total of seventy-five specimens were prepared as presented in Table 3.2, but only fifty-seven were tested because specimens were broken during demolding.

It is assumed that the chemical adhesion progresses with the pullout, and when it detaches throughout the entire embedded length, the load decreases once. The surface of the fiber is somewhat roughened and has irregularities after the chemical adhesion is detached. The frictional resistance to pullout is polarized depending on the degree of irregularities, leading to two scenarios: an increase in load followed by rupture, or a gradual decrease in load as the fiber continues to be pulled out from the matrix. Here, the load and slip at the loss of chemical adhesion are defined as the first peak load (P_a) and slip (S_a), and the maximum load and slip as P_{max} and S_{max}, respectively. These experimental values are presented in Tables 3.3 to 3.5. The failure mode is categorized into pullout (S) and rupture (R). For determining the failure mode rapid load reduction was considered as a reference for the ruptured specimens.

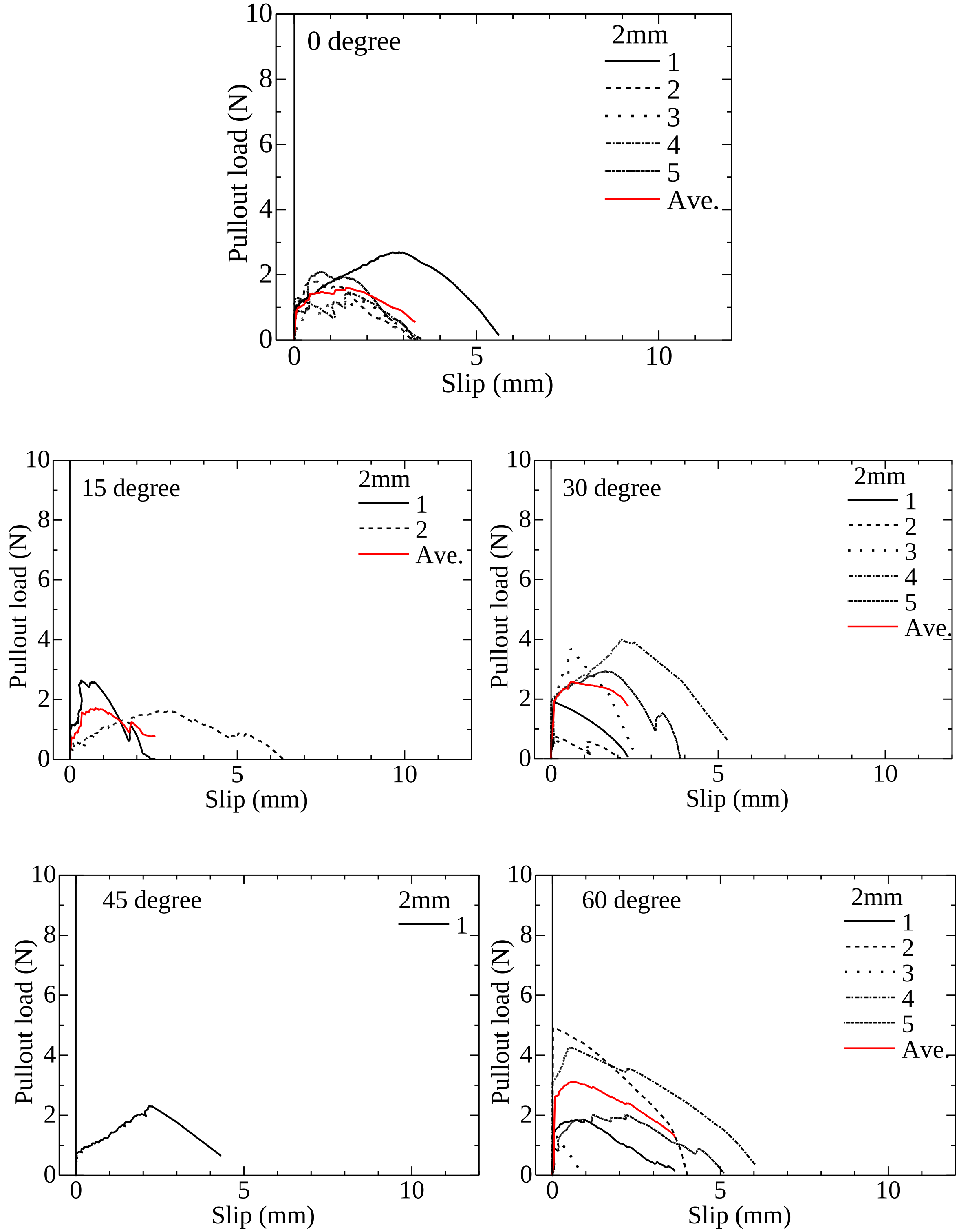

Figure 3.6 Pullout load-slip relationship:
(Embedded length of 6mm, Inclined angle 0°, 15°, 30°, 45°, 60°)

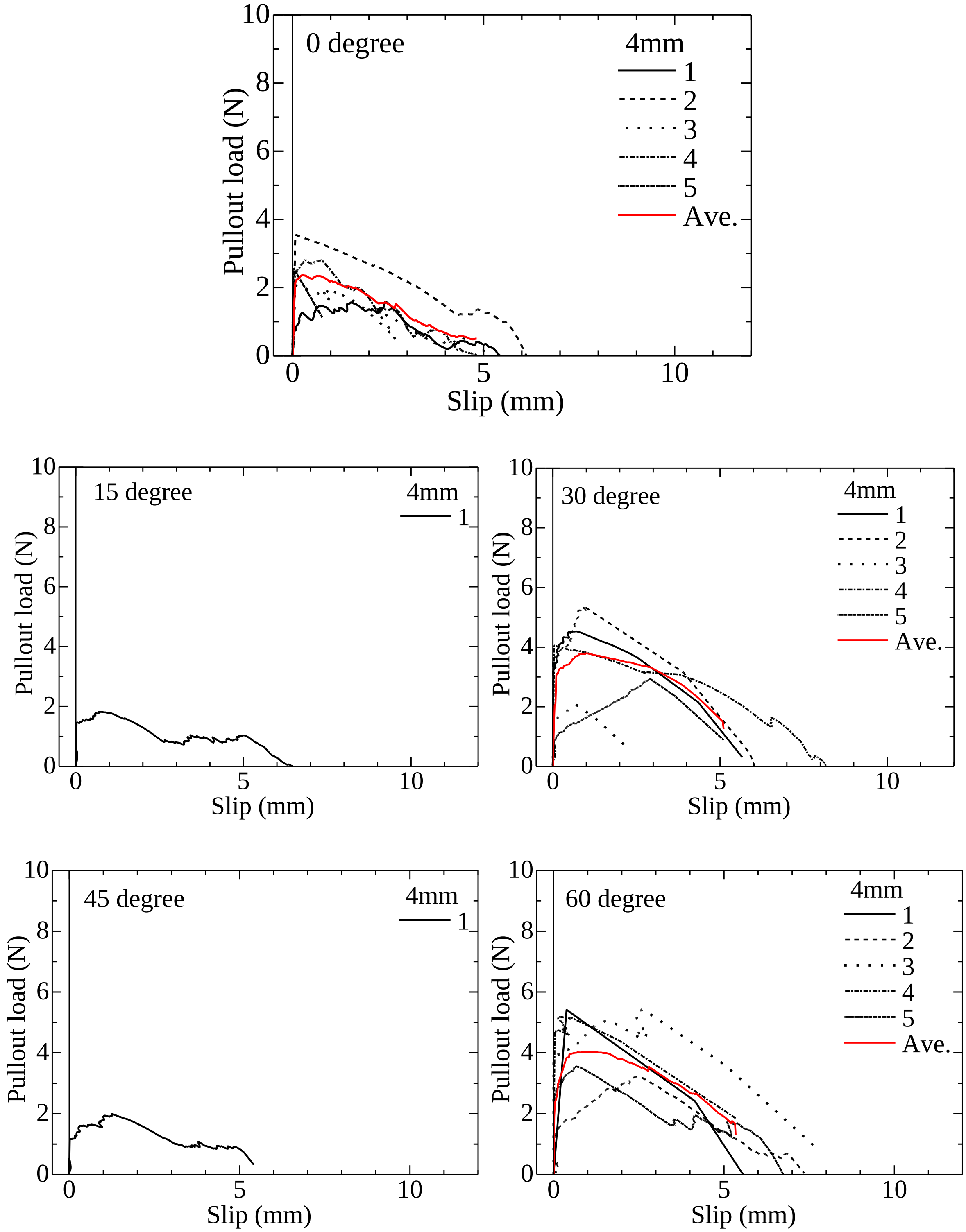

Figure 3.7 Pullout load-slip relationship:
(Embedded length of 4mm, Inclined angle 0°, 15°, 30°, 45°, 60°)

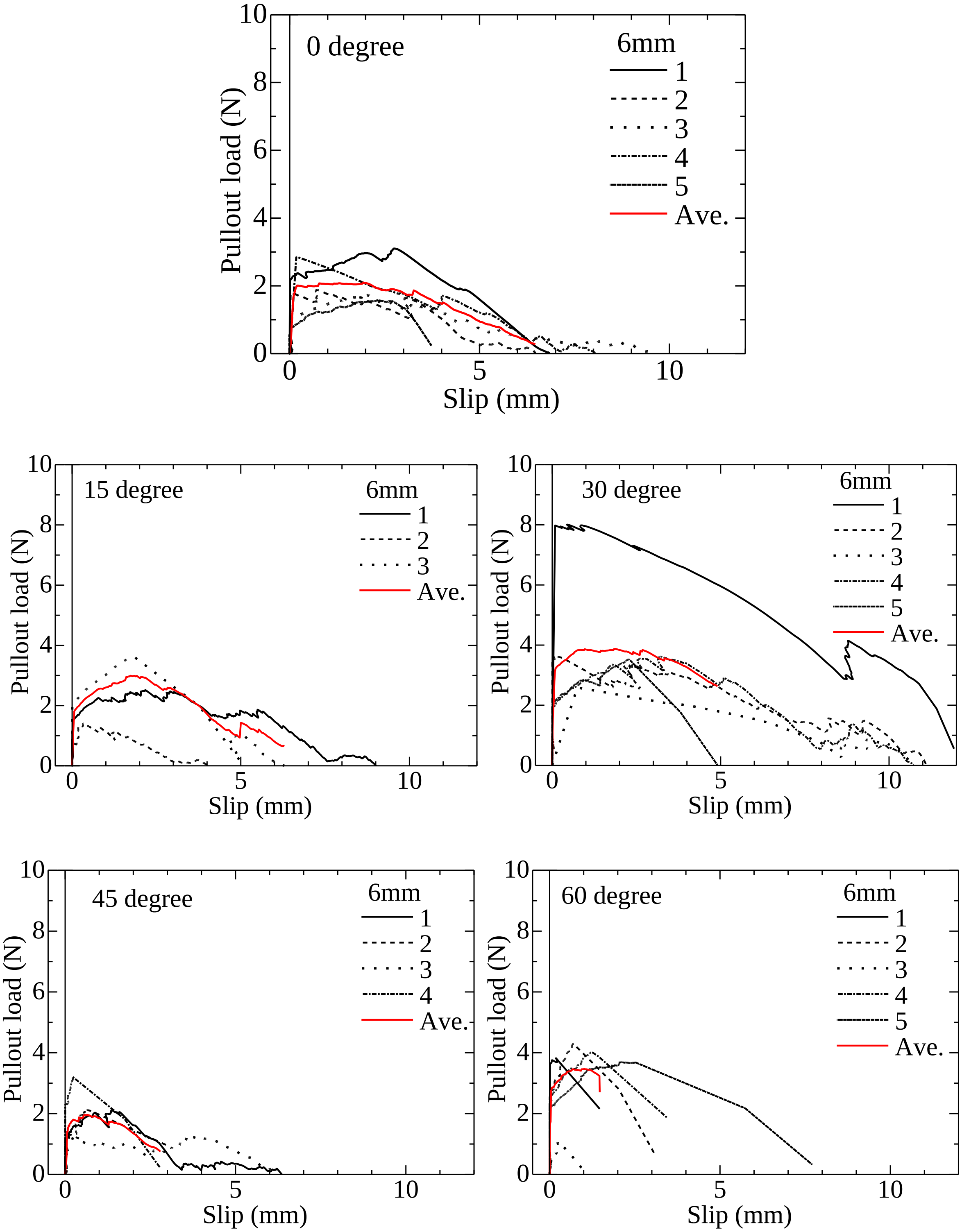

Figure 3.8 Pullout load-slip relationship:
(Embedded length of 6mm, Inclined angle 0°, 15°, 30°, 45°, 60°)

Table 3.3 Pullout test results for 2mm embedded length

Name	Angle of inclination (°)	Embedded length (mm)	P_a (N)	P_{max} (N)	S_a (mm)	S_{max} (mm)	Failure mode
2mm-0-1	0°	2.06	0.96	2.69	0.039	2.880	S
2mm-0-2		2.06	0.86	1.79	0.006	0.352	S
2mm-0-3		2.06	0.89	1.18	0.312	1.921	S
2mm-0-4		2.06	1.29	1.45	0.028	1.545	S
2mm-0-5		2.06	0.85	2.10	0.088	0.717	S
2mm-15-1	15°	2.10	1.15	2.64	0.104	0.340	S
2mm-15-2		2.10	0.55	1.62	0.100	2.677	S
2mm-30-1	30°	2.03	1.91	1.91	-*	0.071	S
2mm-30-2		2.03	0.47	0.74	0.082	0.123	S
2mm-30-3		2.03	1.98	3.69	0.116	0.582	R
2mm-30-4		2.03	2.00	4.00	0.048	2.087	R
2mm-30-5		2.03	2.05	2.93	0.156	1.619	S
2mm-45-1	45°	1.90	0.68	2.30	0.017	2.268	S
2mm-60-1	60°	2.01	1.39	1.84	0.040	0.704	S
2mm-60-2		2.01	4.93	4.93	-	0.017	S
2mm-60-3		2.01	1.44	1.44	-	0.013	S
2mm-60-4		2.01	3.19	4.25	0.064	0.535	S
2mm-60-5		2.01	0.92	2.01	0.046	1.224	S

* $P_a = P_{max}$ and the values of S_a and S_{max} are the same.

Table 3.4 Pullout test results for 4mm embedded length

Name	Angle of inclination (°)	Embedded length (mm)	P_a (N)	P_{max} (N)	S_a (mm)	S_{max} (N)	Failure mode
4mm-0-1	0	4.05	1.22	1.59	0.218	2.422	S
4mm-0-2		4.05	3.55	3.55	-*	0.074	S
4mm-0-3		4.05	2.07	2.07	-	0.072	S
4mm-0-4		4.05	2.59	2.82	0.197	0.733	S
4mm-0-5		4.05	2.58	2.58	-	0.019	R
4mm-15-1	15	4.05	1.46	1.82	0.103	0.750	S
4mm-30-1	30	4.09	3.29	4.53	0.060	0.705	S
4mm-30-2		4.09	3.66	5.39	0.061	0.901	R
4mm-30-3		4.09	1.54	2.07	0.038	0.685	R
4mm-30-4		4.09	4.05	4.05	-	0.036	S
4mm-30-5		4.09	0.89	2.93	0.085	2.901	R
4mm-45-1	45	4.05	1.16	1.99	0.067	1.250	S
4mm-60-1	60	4.10	5.42	5.42	-	0.378	R
4mm-60-2		4.10	1.18	3.21	0.022	2.372	S
4mm-60-3		4.10	3.89	5.44	0.056	2.620	R
4mm-60-4		4.10	4.72	5.18	0.113	0.200	S
4mm-60-5		4.10	2.49	3.55	0.027	0.665	S

* $P_a = P_{max}$ and the values of S_a and S_{max} are the same.

Table 3.5 Pullout test results for 6mm embedded length

Name	Angle of inclination (°)	Embedded length (mm)	P_a (N)	P_{max} (N)	S_a (mm)	S_{max} (mm)	Failure mode
6mm-0-1	0	6.12	2.17	3.10	0.020	2.746	S
6mm-0-2		6.12	1.77	1.88	0.060	0.727	S
6mm-0-3		6.12	1.72	1.72	0.033	2.040	S
6mm-0-4		6.12	2.86	2.86	-*	0.175	S
6mm-0-5		6.12	0.78	1.58	0.086	2.306	R
6mm-15-1	15	6.03	1.46	2.52	0.024	2.171	S
6mm-15-2		6.03	0.67	1.40	0.021	0.324	S
6mm-15-3		6.03	1.97	3.60	0.005	1.863	R
6mm-30-1	30	6.06	8.31	8.31	-	0.453	S
6mm-30-2		6.06	3.66	3.66	-	0.040	S
6mm-30-3		6.06	3.20	3.20	-	0.745	S
6mm-30-4		6.06	1.95	3.62	0.056	3.211	S
6mm-30-5		6.06	2.04	3.52	0.022	2.271	R
6mm-45-1	45	6.06	1.61	2.12	0.373	1.360	S
6mm-45-2		6.06	1.32	2.11	0.100	0.659	R
6mm-45-3		6.06	1.24	1.24	-	0.052	S
6mm-45-4		6.06	2.30	3.21	0.072	0.220	R
6mm-60-1	60	6.08	3.82	3.82	-	0.188	R
6mm-60-2		6.08	2.70	4.30	0.048	0.695	R
6mm-60-3		6.08	0.53	1.09	0.134	0.251	R
6mm-60-4		6.08	2.61	4.02	0.069	1.239	R
6mm-60-5		6.08	2.26	3.69	0.152	2.100	R

* $P_a = P_{max}$ and the values of S_a and S_{max} are the same.

Chapter 4 Single Fiber Pullout Model

4.1 Evaluation of Pullout Load

4.1.1 Specimens with 0-degree inclination

The relationship between the first peak load (P_a) and the maximum load (P_{max}) to the embedded length for specimens with a 0-degree angle of inclination is shown in Figure 4.1. The plot shows the averaged value of the pullout load of the specimens in which their failure mode is pullout (S). A power relationship is adopted for the relationship between the first peak load and maximum load with the embedded length. The approximate equations obtained through the least square method are represented with dashed lines in the figures.

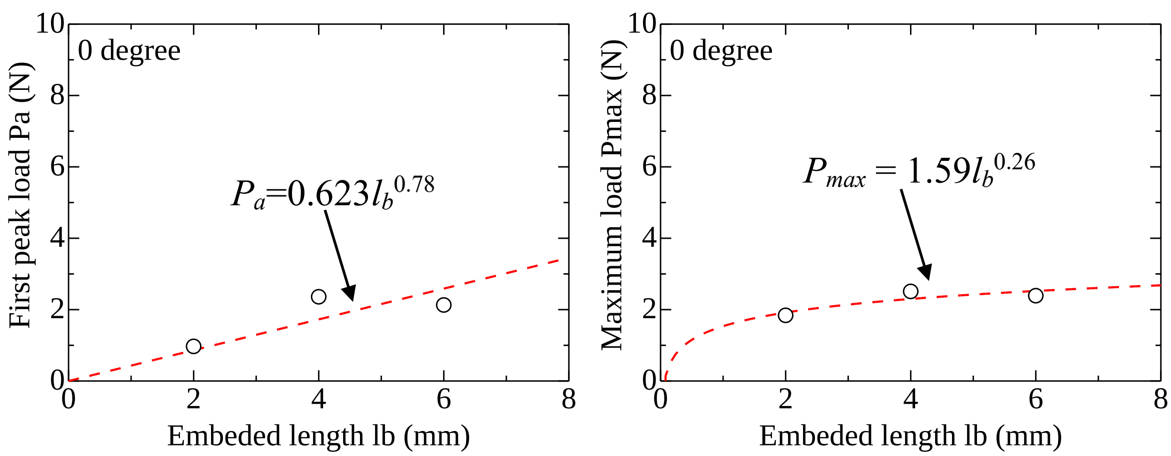

Figure 4.1 Estimation of the first peak and maximum pullout load as a function of embedded length for 0-degree angle of inclination

4.1.2 Specimens with inclination angle

The relationship between the first peak load (P_a) and the maximum load (P_{max}) to the embedded length for specimens with various angles of inclination is shown in Figure 4.2. The plot shows the averaged value of the pullout load of the specimens in which their failure mode is pullout (S). Specimens with 15 and 45 angles of inclination contain fewer numbers due to specimen failure before loading. For specimens with some series of inclination angles, an increase in the first peak load and the maximum load with the increase in the inclination angle and embedded length was observed. For specimens with fewer number series, a clear increase was not distinctly observed.

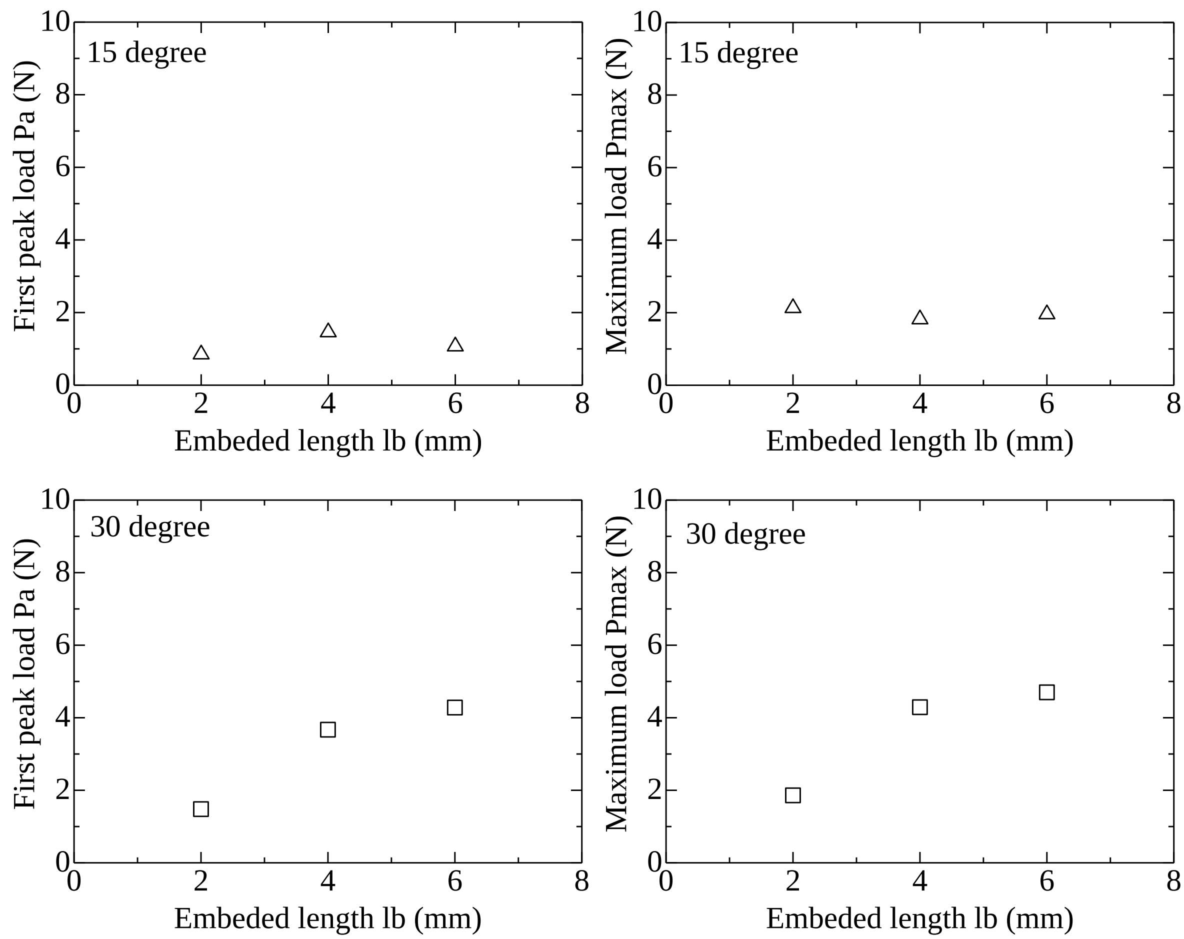

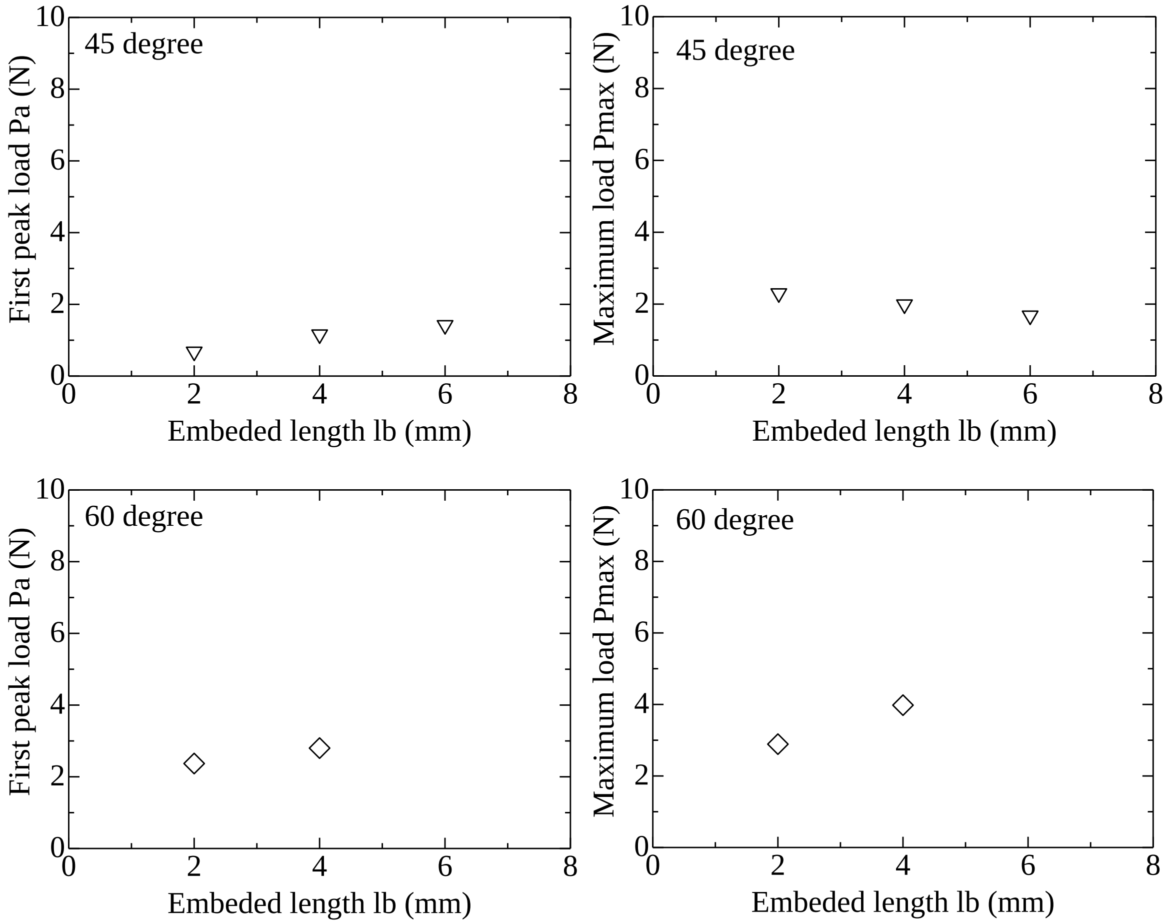

Figure 4.2 First peak and maximum pullout load - embedded length relationship for 15, 30, 45, and 60 degrees of inclination

4.2 Evaluation of Slip

4.2.1 Specimens with 0-degree inclination

The relationship between slip values, S_a, at the first peak load and S_{max} at the maximum load, and the embedment length for 0-degree inclination angle is shown in Figure 4.3. A linear relationship is adopted for the relationship between slip at the first peak load, S_a, and slip at the maximum load, S_{max}, with the embedded length. The approximate equations obtained through the least square method are represented with dashed lines in the figures.

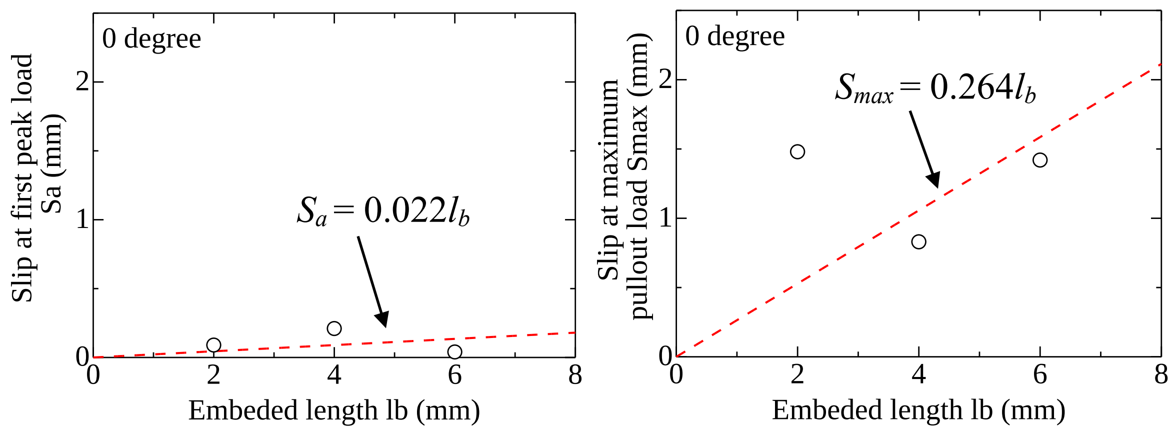

Figure 4.3 Estimation of slip at first peak and maximum pullout load as a function of embedded length for 0-degree angle of inclination

4.2.2 Specimens with inclination angle

The relationship between slip values, S_a, at the first peak load and S_{max} at the maximum load, and the embedment length for various inclination angles is shown in Figure 4.4. As the inclination angle increases, there is an apparent increase in the slip at the maximum load for specimens with embedding angle variation. The figure does not show a clear correlation between slip values and embedment length. The significant variability in experimental data makes it challenging to assess correlations for each parameter individually.

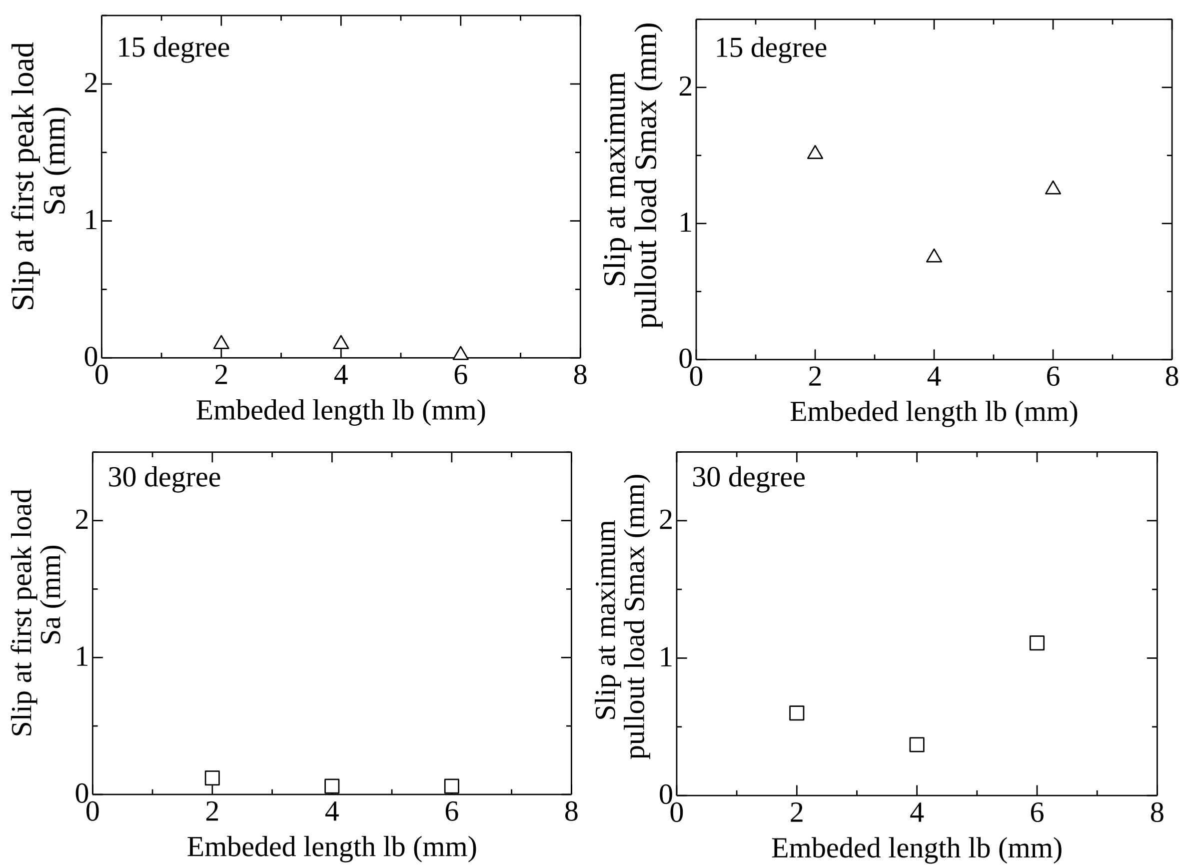

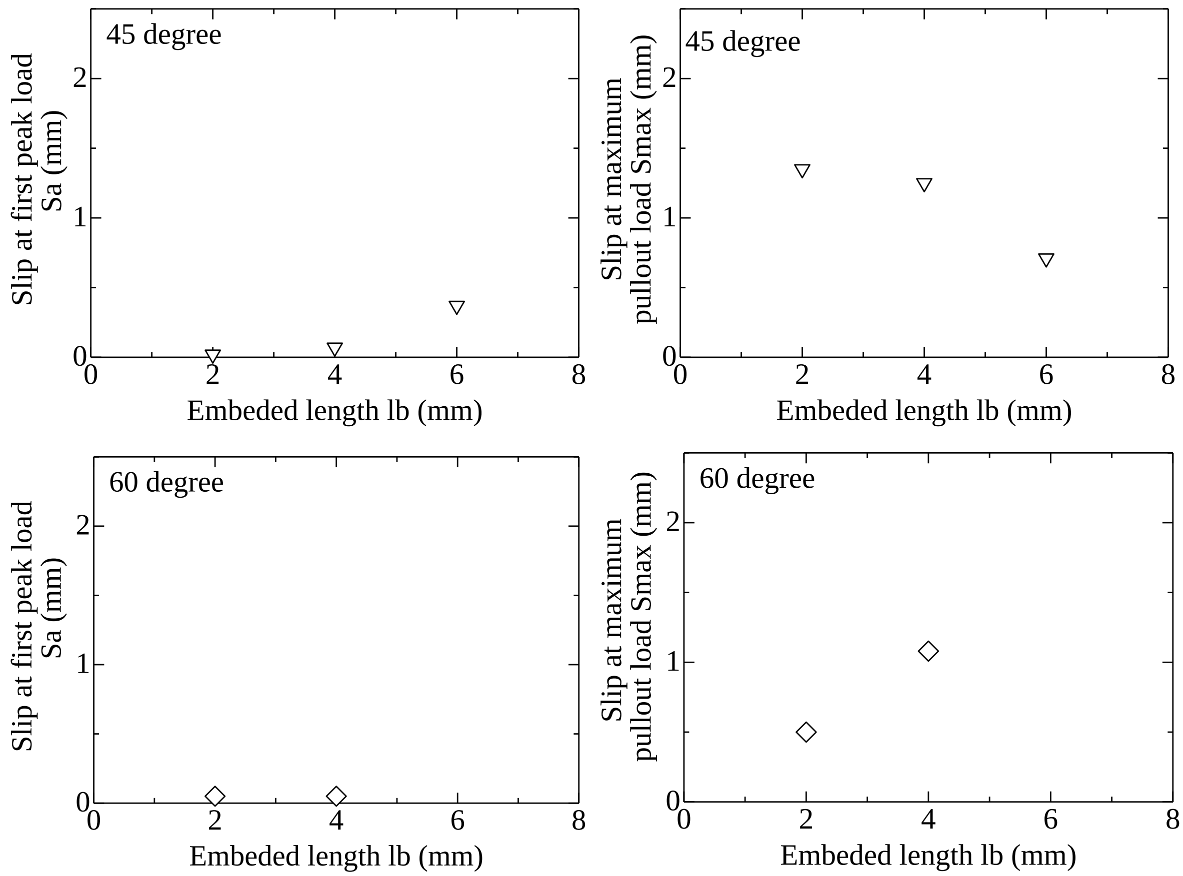

Figure 4.4 Slip at first peak and maximum pullout load - embedded length relationship for 15, 30, 45, and 60 degrees of inclination

4.3 Snubbing Effect

In FRCC, when fibers have an orientation angle (θ), a snubbing effect has been reported in previous studies [9,15]. This effect leads to an apparent increase in pullout resistance due to concentrated reaction forces at the fiber embedding edge. To quantitatively express the snubbing effect, a snubbing coefficient (f) has been introduced. The maximum pullout load, accounting for the snubbing effect, can be represented using the snubbing coefficient in the form of Equation (4.1).

$$P_{max} = P_0 \cdot e^{f\theta} \tag{4.1}$$

Where,

P_{max}: maximum pullout load
P_0: P at inclination angle of 0
f: coefficient of the snubbing effect for pullout load
θ: inclination angle

As shown in Equation (4.1), the definition of the snubbing coefficient indicates the degree of increase in the maximum pullout load. However, when the fiber ruptures before reaching the maximum pullout load, the load value cannot be evaluated. In the case of determining the snubbing coefficient from experimental results, the data for ruptured loads need to be excluded. For the first peak load, the first peak load P_a is normalized by the average of the first peak load $P_{a,0}$ for specimens with an inclination angle of 0°. The relationship between the normalized load and the inclination angle is shown in Figure 4.5. The unit of the inclination angle θ is in radian when calculating the coefficient related to the snubbing effect f. The curves in the figure represent the results of approximating Equation (4.1) using the least squares method, yielding a snubbing coefficient of 0.31. Similarly, for the maximum pullout load, the relationship between the normalized load and the inclination angle is illustrated in Figure 4.6, resulting in a snubbing coefficient of 0.42. In both cases, the snubbing coefficients are nearly similar, suggesting that the influence of the first peak load is also a significant factor in determining the snubbing coefficient. The average of the two is used in the bridging law calculation in Chapter 5.

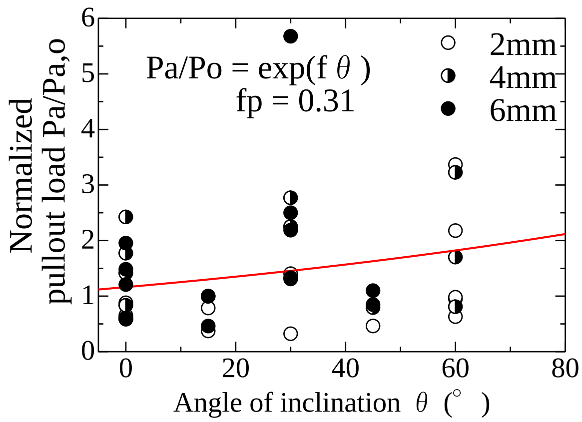

Figure 4.5 Snubbing coefficient at first peak load

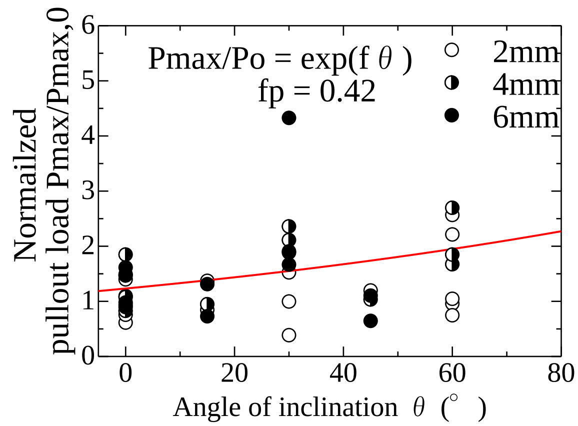

Figure 4.6 Snubbing coefficient at maximum pullout load

4.4 Apparent Strength of Fibers

In the pullout test, fiber ruptures were observed in some specimens. The reduction of apparent fiber strength due to surface roughening is expressed using the fiber strength reduction coefficient f' in the following equation:

$$\sigma_{fu} = \sigma^{n}{}_{fu} \cdot e^{-f' \cdot \Phi} \tag{4.2}$$

Where:

σ_{fu}: apparent strength of fiber

$\sigma^{n}{}_{fu}$: rupture strength of the fiber at angle $\phi = 0$

f': apparent fiber strength reduction factor

Φ: inclination angle

The relationship between the rupture strength, calculated by dividing the maximum pullout load in specimens with confirmed fiber ruptures by the average fiber cross-sectional area, and the inclination angle is illustrated in Figure 4.7. The solid line in the figure represents the fitted curve. The intercept of the fitted equation, 110 MPa, corresponds to the apparent fiber strength when the angle of inclination is 0 and the coefficient -0.006 is considered as the fiber strength reduction coefficient f'. Previous studies [9] reported a decrease in rupture strength with an increasing inclination angle, but experimental results show that the rupture strength increases with a larger inclination angle. This discrepancy is expected to be due to the fiber breaking during the process of increased pullout load due to the snubbing effect and the chemical composition of the natural fiber.

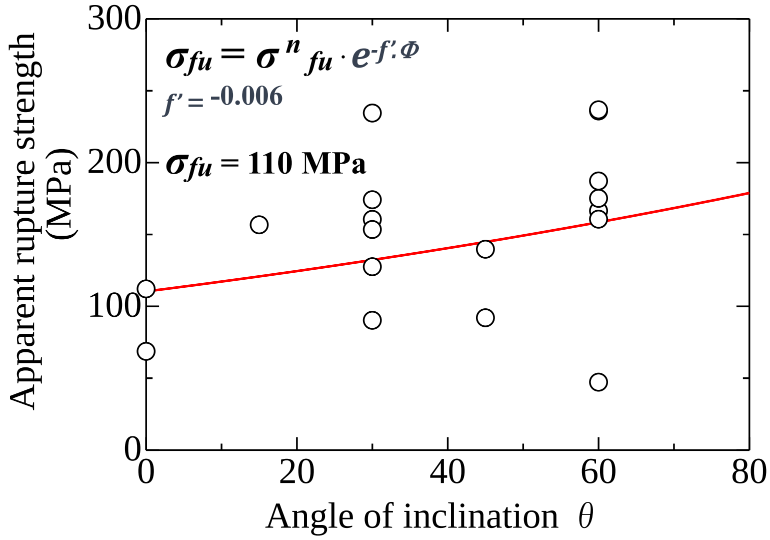

Figure 4.7 Apparent rupture strength of palm fiber

4.5 Trilinear Model of Pullout – Slip Curve

Based on the experimental results presented in the previous sections, modeling the bridging law of a single fiber is conducted. By summing the modeled bridging laws of single fibers, it becomes possible to calculate the bridging law at any cross-section of a given specimen. The pullout–slip curve of a single fiber is modeled using a trilinear model with three linear segments, as illustrated in Figures 4.8 and 4.9.

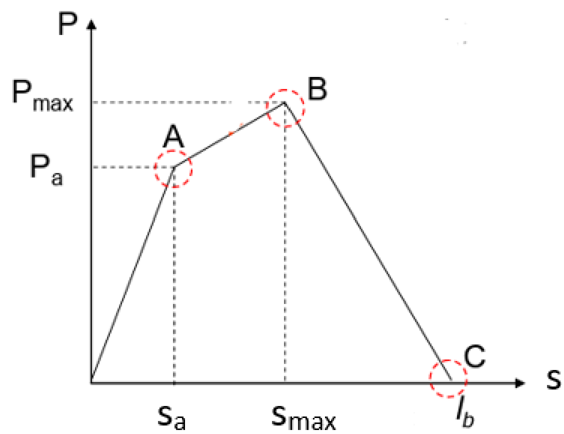

Figure 4.8 Trilinear Model

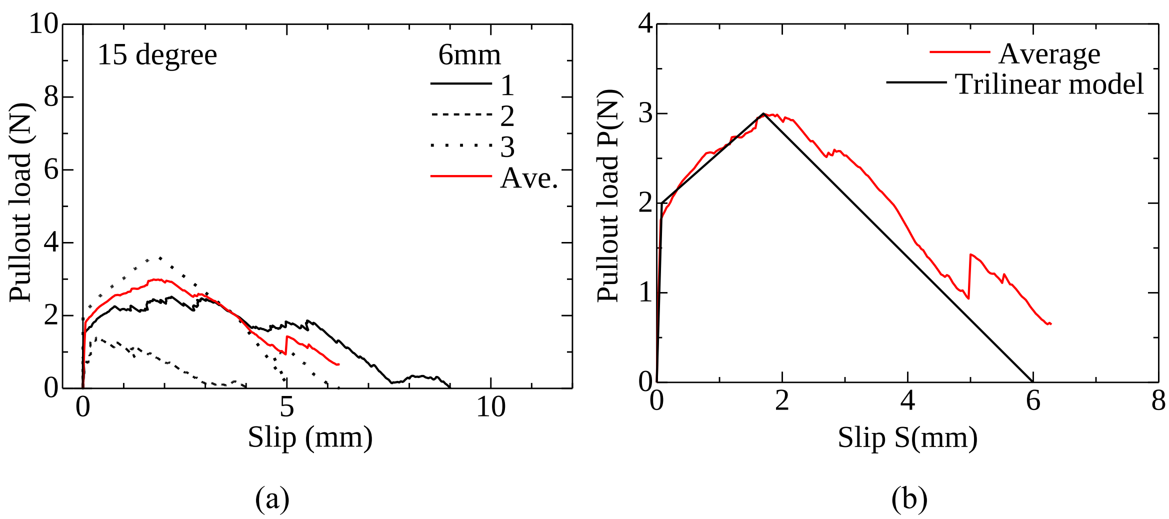

Figure 4.9 Example of trilinear model:

(a) Experiment result, (b) Model result

The first peak load (P_a) is the load at the point when the detachment of chemical adhesion occurs across the entire embedded length during the single fiber pullout test. After the first peak, the load increases due to frictional resistance, reaching the maximum load (P_{max}). Further pullout leads to load loss when the slip reaches the embedded length (l_b).

From Figures 4.1 and 4.3 the first peak load, the maximum pullout load, the slip at the first peak load, and the slip at the maximum pullout load are expressed in Equations (4.3) to (4.6).

$$P_a = 0.62 l_b^{0.78} \tag{4.3}$$

$$P_{max} = 1.6 l_b^{0.26} \tag{4.4}$$

$$S_a = 0.02 l_b \tag{4.5}$$

$$S_{max} = 0.26 l_b \tag{4.6}$$

Chapter 5 Modeling of Bridging Law

5.1 Calculation Method

In this chapter, a bridging model based on the single-fiber pullout load-slip model is employed to perform bridging law calculations. The bridging law can be obtained by the summation of forces carried by individual bridging fibers considering the probability density function (PDF) for the fiber inclination angle and the fiber centroidal location [6] as given in Equation (5.1).

$$\sigma_{bridge} = \frac{P_{bridge}}{A_m} = \frac{V_f}{A_f} \cdot \sum_h \sum_j \sum_i P_{ij}\left(w,\psi\right) \cdot p_{xy}\left(\theta_i\right) \cdot p_{zx}\left(\phi_j\right) \cdot p_x\left(y_h, z_h\right) \cdot \Delta\theta \cdot \Delta\phi \cdot \left(\Delta y \cdot \Delta z\right) \tag{5.1}$$

Where,

σ_{bridge} = bridging stress,
P_{bridge} = bridging force (= total of pullout load),
A_m = cross-sectional area of matrix,
V_f = fiber volume fraction,
A_f = cross-sectional area of an individual fiber,
$P(w,\psi)$ = pullout load of an individual fiber,
P_{xy}, P_{zx} = probability density function for fiber inclination angle,
P_x = probability density function for fiber centroidal location,
ψ = fiber inclination angle to x-axis (= max$\{\theta, \phi\}$),
θ = angle between x-axis and projected line of the fiber to x-y plane,
ϕ = angle between x-axis and projected line of the fiber to z-x plane,
w = crack width.

In the bridging model, crack width is determined, by assuming that fibers bridging the crack surface are pulled out from the side with a shorter embedment length on the crack surface [16]. The crack width at the time of the first peak pullout load is set as 2 times the slip at the time of the first peak pullout load and is expressed by Equation (5.2). The maximum crack width at the time of maximum pullout load is set as 1.5 times the slip at the time of maximum pullout load and is expressed by Equation (5.3).

$$\delta_a = 2 \times S_a = 0.04 l_b \tag{5.2}$$

$$\delta_{max} = 1.5 \times S_{max} = 0.4 l_b \tag{5.3}$$

5.2 Calculation Parameters

Table 5.1 shows the parameters for the calculation of bridging law. The calculation is conducted using a trilinear model for the pullout load-crack width relationship of an individual fiber. In addition, inclined fiber angle and rupture of fiber are also considered in the calculation. The orientation intensity k in the elliptic distribution for the PDF of the fiber inclination angle is set to be 1 for the two planes parallel to the axial direction. Furthermore, the principal orientation angle θ_r is set to be 0.

Table 5.1 Parameters for the calculation of bridging law

Parameter		Input
Cross-sectional area of individual fiber, A_f (mm^2)		0.023
Length of fiber, l_f (mm)		12
fiber volume fraction		0.025
Snubbing coefficient		0.35
Apparent rupture strength of fiber, MPa		$\sigma_{fu} = 110e^{0.006\Phi}$
Trilinear model	Maximum pullout load, P_{max} (N)	$P_{max} = 1.6 l_b^{0.26}$
	First peak load, P_a (N)	$P_a = 0.62 l_b^{0.78}$
	Crack width at P_{max}, W_{max} (mm)	$W_{max} = 0.4 l_b$
	Crack width at P_a, W_a (mm)	$W_a = 0.04 l_b$
Elliptic distribution	Orientation intensity for x-y plane k_{xy}	1
	Orientation intensity for z-x plane k_{zx}	1
	Principal orientation angle θ_r	0

The fibers were prepared using a shredder resulting that the length of the fibers is not constant. Thirty samples of fiber were measured using a ruler as shown in Figure 5.1. Figure 5.2 shows the distribution of the fiber length with an average length of 12mm.

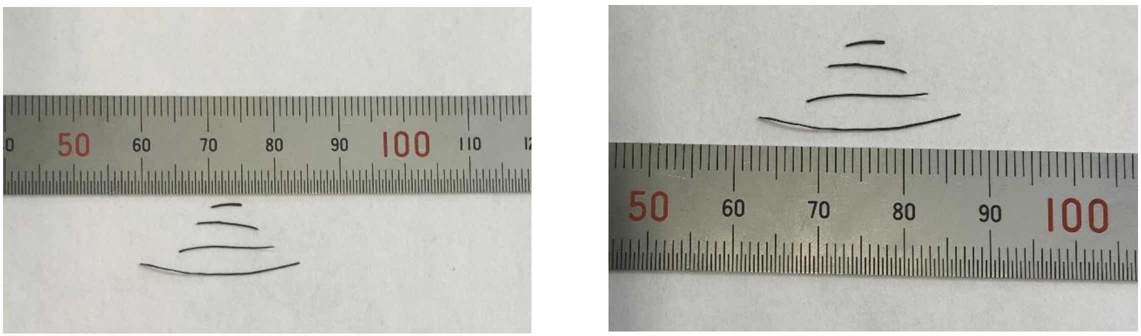

Figure 5.1 Fiber length measurement

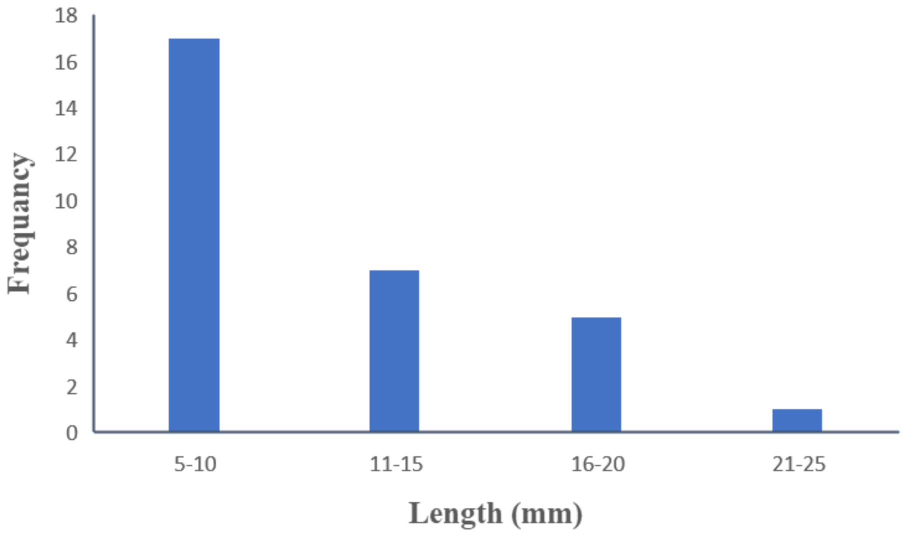

Figure 5.2 Fiber length distribution

5.3 Calculation Results

The results of the bridging law calculations are shown in Figure 5.3. The relationship between fiber efficiency ($N_{f,b}/N_f$) and crack width from the bridging law calculation is shown in Figure 5.3b. Fiber efficiency represents the ratio of the number of effective bridging fibers, those not pulled out or ruptured and supporting bridging forces, denoted as $N_{f,b}$ to the theoretical number of fibers N_f within a unit volume. In Figure 5.3a it is observed that the tensile stress approaches zero before the crack width reaches half of the length of the fiber, 6mm, it is assumed that most of the fibers are ruptured before being fully pulled out of the matrix.

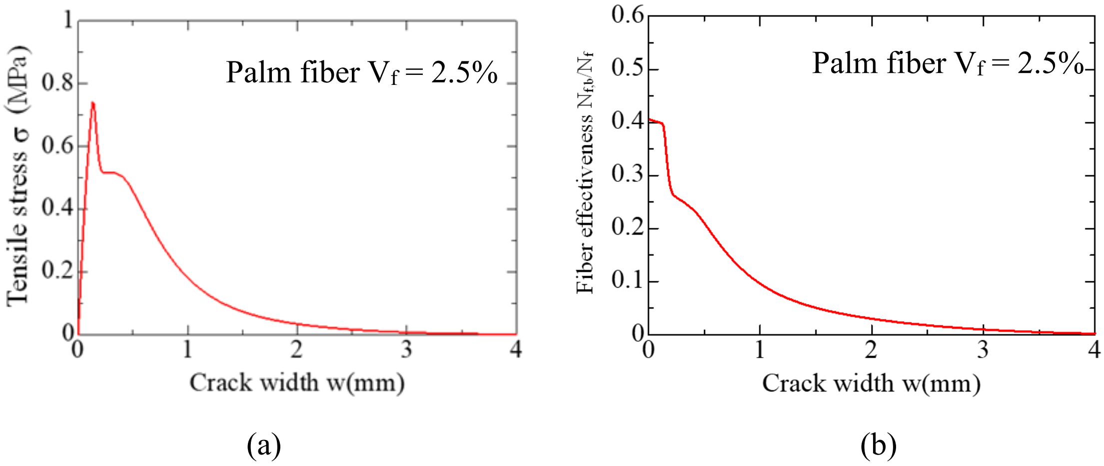

Figure 5.3 Calculation result of bridging law

(a) Tensile stress – crack width, (b) Fiber effectiveness- crack width

5.4 Suitability Assessment of Modeled Bridging Law

5.4.1 4-point bending test

A four-point bending test with a pure bending length of 100 mm using a 500kN universal testing machine is carried out to investigate the flexural characteristics of palm-FRCC. The specimen was a prism with a cross-section of 100mm×100mm and a length of 400mm and three specimens each, for mortar (N) and with a 3% fiber volume fraction(P3%), were prepared. The materials used are the same as those described in section 3.1.1. Two π-type LVDTs are affixed to the front surface of the specimen to measure axial deformations in the constant bending moment region as shown in Figure 5.4. The average curvature is determined from the disparity between upper and lower strains caused by axial deformations.

A compression test using ϕ100-200mm cylinder test pieces for specimens without fiber and specimens with a fiber volume fraction of 3% is conducted and the results are shown in Table 5.2.

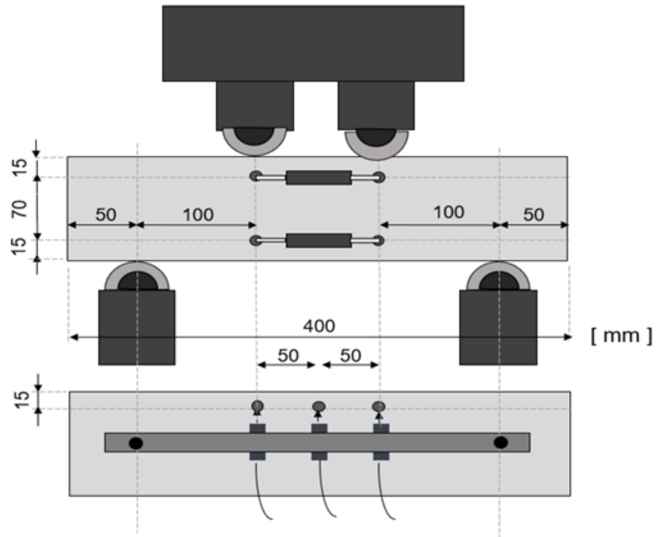

Figure 5.4 Four-point bending test setup

Table 5.2 Compressive strength and elastic modulus

Specimen	Compressive strength (MPa)	Elastic modulus (GPa)
N	26.0	12.5
P 3%	25.2	11.8

5.4.2 Section analysis

The fiber volume fraction was initially set to 3% during the 4-point bending test. However, it's important to note that the fibers were prepared using a shredder, and some of them turned out to be very small. Given their size, their impact on bridging characteristics was assumed to be negligible. To quantify this, the percentage of these small fibers was determined by analyzing the weight difference of samples before and after passing through a 2mm diameter sieve. Five samples were used, and the weights were measured, as illustrated in Figure 5.5. The excluded fiber percentage, based on the weight difference, was found to be 15%, as indicated in Table 5.3. For analysis purposes, by excluding 15% of the fiber volume fraction from that used in the 4-point bending test, the fiber volume fraction was set to 2.5%.

Figure 5.5 Quantification of the smaller-size fibers

Table 5.3 Calculation of actual fiber volume fraction for bridging law

Sample	Weight of fiber (g)	Weight of fiber after 2mm sieve (g)
1	4.71	0.65
2	6.17	0.88
3	5.06	0.82
4	8.55	1.13
5	6.52	0.96
Avg.	6.20	0.89
	Percentage of smaller fibers	14.3%

Section analysis is conducted to assess the adaptability of the modeled bridging law calculations in Section 5.3. The section analysis is carried out based on the assumption that a plain section remains plain. The trilinear stress–strain models for section analysis is shown in Figure 5.6. Parabolic curves are chosen for the compressive stress–strain model, with the compressive strengths and strains at the maximum derived from the compression test results. The points σ_{max}, σ_2, ε_{max}, ε_2, and ε_u in the tensile stress–strain models are defined by previously calculated bridging laws.

$$\varepsilon_{max} = \frac{\delta_{max}}{l}$$

$$\varepsilon_2 = \frac{\delta_2}{l}$$

$$\varepsilon_u = \frac{\delta_u}{l}$$

Where,

σ_{max}, σ_2, δ_{max}, δ_2 and δ_u = parameter of trilinear model of bridging law

l = length of pure bending moment area in 4-point bending test (=100mm)

σ_{max} = 0.742MPa

σ_2 = 0.517MPa

δ_{max} = 0.006mm

δ_2 = 0.3mm

δ_u = 3.5mm

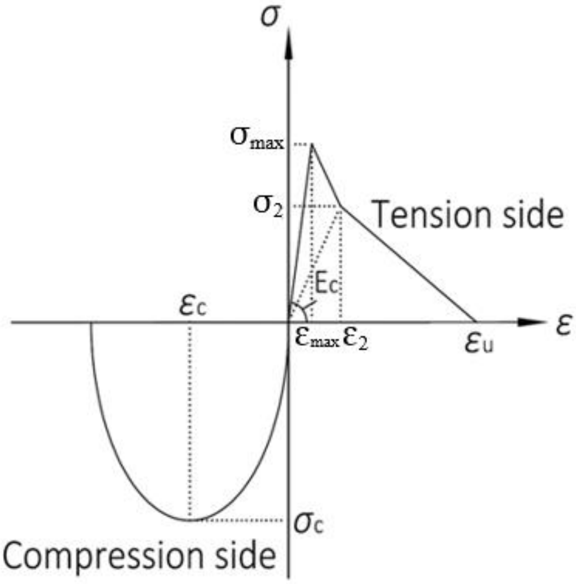

Figure 5.6 Stress - strain model applied in section analysis

5.4.3 Comparison of Analysis and Experimental Results

Figure 5.7 shows the bending moment M - curvature φ relationship, where the black lines show the experimental results obtained from the 4-point bending test, and the red lines show the analysis results. As shown in Figure 5.7, the analysis result shows good agreement with the experimental results.

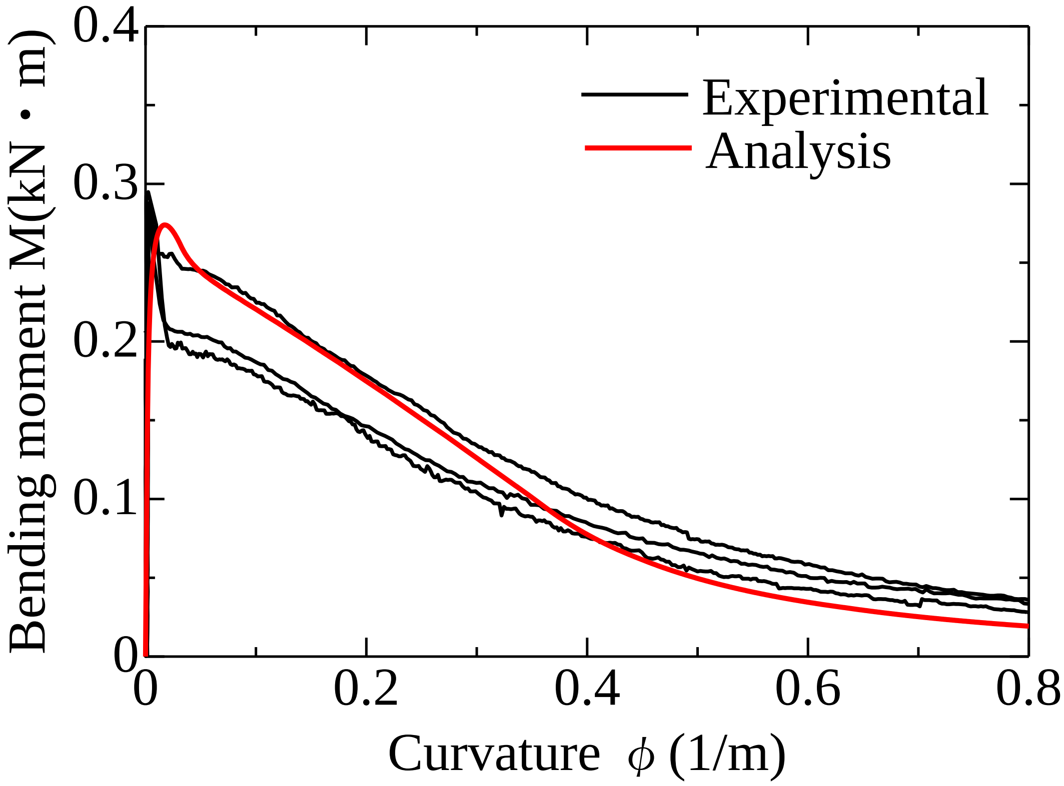

Figure 5.7 Bending moment – curvature relationship

5.4.4 Effect of fiber volume fraction

To examine the effect of fiber volume fraction on the tensile characteristics, a bridging law calculation was done for different fiber volume fractions. As revealed in Figure 5.8, the increase in fiber volume fraction (V_f) results in the increase of the tensile stress, which is directly proportional to the crack-bridging characteristics of the fiber.

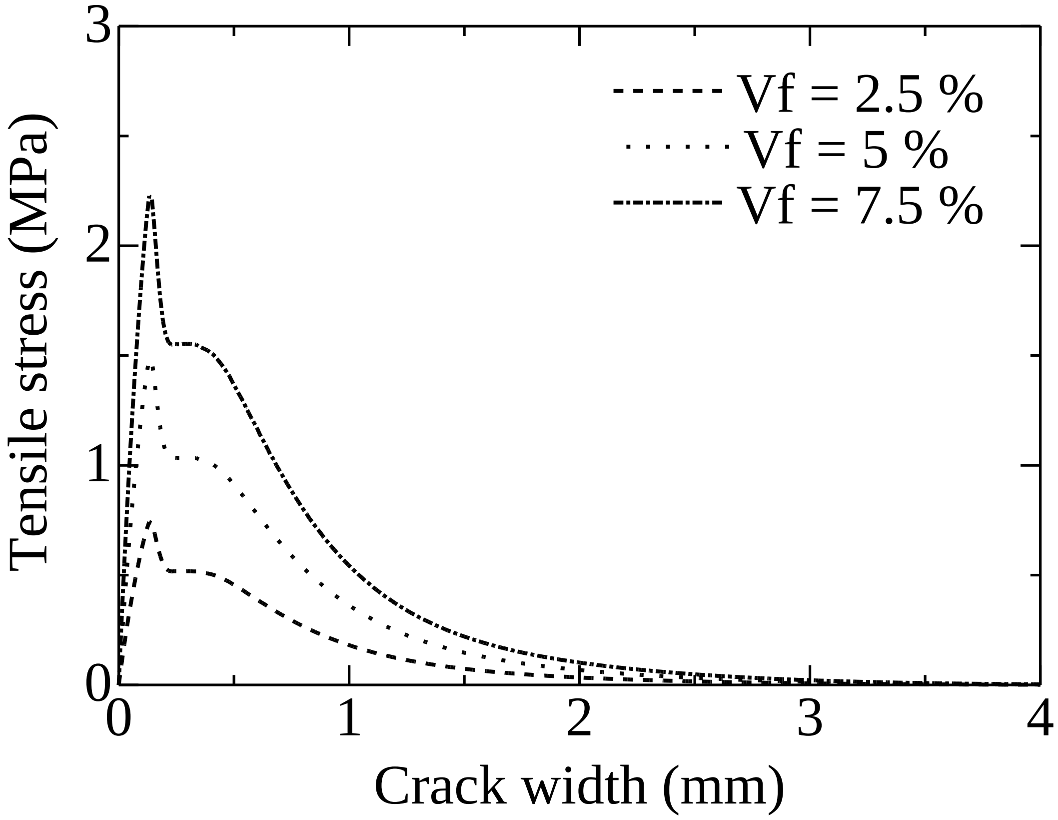

Figure 5.8 Tensile stress - crack width relationship

Chapter 6 Conclusion

To investigate the crack-bridging behavior of palm fiber in FRCC, a single fiber pullout test of palm fibers was conducted. The pullout test was performed for specimens with and without inclination angles. Pullout load–slip curves were modeled based on the results of the single fiber pullout test and the calculation of bridging law was conducted. The adaptability of bridging law was assessed using a section analysis for a four-point bending test. The following conclusions are drawn based on the results:

1. In the single fiber pullout test result, a clear fiber rupture or matrix damage was not observed. Even though there is variability in the experimental results, a correlation between the slip, embedded length, and angle of inclination was confirmed to some extent.

2. A power function relationship between the first peak load and the maximum pullout load with embedded length was found for specimens with 0-degree angle of inclination. Whereas a linear function relationship was adopted between the slip at the first peak load and at the maximum pullout load with the embedded length.

3. The relationship between the normalized pullout load and the inclination angle was examined based on the experimental results. Snubbing effects were considered for the first peak load and maximum pullout load.

4. The pullout behavior of a single fiber was modeled using a trilinear model. A tensile stress–crack width relationship model for palm-FRCC was created using the bridging law calculation based on the trilinear model.

5. Section analysis is conducted to assess the adaptability of the modeled bridging law calculations. The analysis result of the bending moment – curvature relationship shows good agreement with the experimental results obtained from the 4-point bending test of palm-FRCC.

Acknowledgments

I would like to express my sincere gratitude to all those who have contributed to the completion of this thesis. This journey has been challenging yet immensely rewarding, and I am deeply thankful for the support and encouragement I have received.

First and foremost, I extend my heartfelt appreciation to my academic supervisor, Toshiyuki Kanakubo, for his invaluable guidance, unwavering support, pleasant communication, and insightful feedback throughout the entire research process. His expertise and encouragement have been instrumental in shaping the direction of this work.

I would like to extend my appreciation to my sub-supervisors, Professor Takahashi Matsushima and Associate professor Akira Yasojima, and Mr. Kojima, a technical staff member, for their valuable time, constructive comments, and thoughtful suggestions. Their collective expertise has significantly enriched the quality of this thesis.

I would also like to thank former and present members at Kanakubo laboratory who have shared their insights and experiences, help with the success of my experiments, and create a nice working environment.

Finally, I would like to express my gratitude to my family, my husband Dr. Alula Tesfay, for their unconditional love, encouragement, and belief in my abilities. Their unwavering support has been my anchor during the highs and lows of this academic journey.

References

1. T. Kanakubo: Tensile Characteristics Evaluation Method for Ductile Fiber-Reinforced Cementitious Composites, Journal of Advanced Concrete Technology Vol. 4, No. 1, 3-17, 2006
2. J. Fangming; T. Likang; Y. Tan; Y. Jiangtao: Tensile strain-hardening cementitious composites and its practical exploration without reinforcement: A review, Frontiers in Materials, 2022
3. NG. Ozerkan; B. Ahsan; S. Mansour; SR. Iyengar: Mechanical performance and durability of treated palm fiber reinforced mortars, International Journal of Sustainable Built Environment 2, 131–142, 2013
4. Sicakova et al.: Effect of selected cellulosic fibers on the properties of cement-based composites, Advanced Materials Letters, 2018
5. Ghanem et al.: Effect of palm fibres addition on absorption characteristics and mechanical properties of concrete, Sustainable Construction Materials and Technologies, 2019
6. T. Kanakubo; M. Miyaguchi; K. Asano: Influence of Fiber Orientation on Bridging Performance of Polyvinyl Alcohol Fiber-Reinforced Cementitious Composite, Materials Journal, American Concrete Institute, Vol.113, No.2, pp.131-141, 2016.
7. Y. Ozu; M. Miyaguchi; T. Kanakubo: Modeling of Bridging Law for PVA Fiber-Reinforced Cementitious Composite Considering Fiber Orientation, Journal of Civil Engineering and Architecture, Volume 12, Number 9, pp.651-661, 2018
8. Li, V.C.: From Micromechanics to Structural Engineering. The Design of Cementitious Composites for Civil Engineering Applications, Journal of Structural Mechanics and Earthquake Engineering, JSCE, Vol.10, No.2, pp.37- 48, 1993
9. Li, V.C. et al.: Effect of Inclining Angle, Bundling, and Surface Treatment on Synthetic Fiber Pull-out from a Cement Matrix, Composites, Vol.21, No.2, pp.132-140, 1990
10. T. Kanda; V.C. Li: Interface Property and Apparent Strength of a High Strength Hydrophilic Fiber in Cement Matrix, Journal of Materials in Civil Engineering, ASCE, Vol.10, No.1, pp.5-13, 1998
11. Alhijazi et al.: Recent Developments in Palm Fibers Composites: A Review, Springer Science+Business Media, 2020
12. M. Adamu; Y. Ibrahim; OS. Ahmed; Q. Drmosh: Mechanical performance of date palm fiber-reinforced concrete modified with nano-activated carbon, Nanotechnology Reviews, vol. 12, no. 1, 2023
13. P.-A. Bonnet-Masimbert, F. Gauvin, H.J.H. Brouwers, S. Amziane: Study of modifications on the chemical and mechanical compatibility between cement matrix and oil palm fibers, Results in Engineering, Volume 7, 2020
14. F. Alatshan; A.M. Altlomate; F. Mashiri; W. Alamin: Effect of date palm fibers on the mechanical properties of concrete, International Journal of Sustainable Building Technology and Urban Development, 8(2), 68-80, 2017

15. V.C. Li; Y. Wang; S. Backer: Effect of inclining angle, bundling and surface treatment on synthetic fiber pull-out from a cement Matrix, Mater. Res. Soc. Symp. Proc. 114, 159-165, 1988
16. T. Kanakubo; S. Echizen; J. Wang; Y. Mu: Pullout Behavior of Bundled Aramid Fiber in Fiber-Reinforced Cementitious Composite", Materials, 13(7), 1746, 2020